1989009877   N89-19248

SOLUTION OF STEADY AND UNSTEADY TRANSONIC-VORTEX FLOWS USING EULER AND FULL-POTENTIAL EQUATIONS

Osama A. Kandil
Andrew H. Chuang
Hong Hu
Old Dominion University
Norfolk, Virginia

OUTLINE OF TALK

1. Background and Objectives

2. Unsteady Euler Equations in a Rotating Frame of Reference for Transonic Vortex Flows:

   - Formulation (Space Fixed and Rotating Frames of Reference)

   - Method of Solution, Local-Conical Flow, Initial and Boundary Conditions

   - Results: ● Symmetric Conical Flow

     ● Three-Dimensional Steady Transonic-Vortex Flow

     ● Uniform Rolling in a Conical Flow

     ● Rolling Oscillation in a Conical Flow

3. Transonic Airfoil Computation Using Integral Solution of Full-Potential Eq. With and Without Embedded Euler Domains:

   - Formulation (I.E. Solution of Full-Potential Eq., Euler Equations)

   - Method of Solution (SCSF-Scheme, IEEE-Scheme)

   - Results: SCSF and IEEE Schemes are Applied to
     NACA 0012 and NACA 64A010A Over a Wide Range of M_∞.

4. Concluding Remarks

1. Background and Objectives

- As the normal angle of attack, normal Mach number and sweep-back angle are varied; complex flows develop around Delta and Delta-like wings.

  These flows are characterized with the formation of large and small scale vortices, weak and strong shock waves, and shock induced separations. The experimental Miller and Wood Classification Diagram shows seven regions of this flow.

- These flows become highly complex when vortex breakdown occurs in the vicinity of the wing or when the wing undergoes unsteady motion due to maneuvering or flutter.

- The main objectives of this ongoing research research work are to develop efficient and reliable computational schemes which are capable of predicting the distributed aerodynamic characteristics of these wings in steady and unsteady flows over a wide range of angles of attack, sweep-back angles, Mach numbers and configurations.
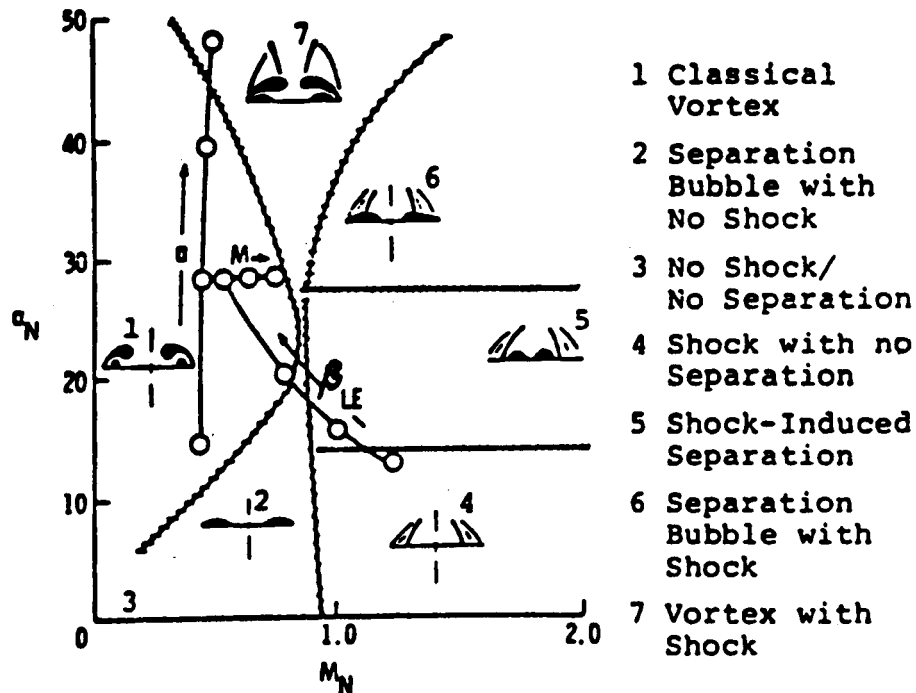

1 Classical Vortex

2 Separation Bubble with No Shock

3 No Shock/ No Separation

4 Shock with no Separation

5 Shock-Induced Separation

6 Separation Bubble with Shock

7 Vortex with Shock

Fig. 1   Miller and Wood[1] Classification Diagram.

2. Unsteady Euler Equations in a Rotating Frame of Reference for Transonic-Vortex Flows

Formulation

● Conservation Form of Euler Equations in a Space-Fixed Frame of Reference

where

$$\frac{\partial \bar{q}}{\partial t} + \frac{\partial \bar{E}}{\partial x} + \frac{\partial \bar{F}}{\partial y} + \frac{\partial \bar{G}}{\partial z} = 0 \qquad (1)$$

$$\bar{q} = [\rho, \rho u, \rho v, \rho w, \rho e]^t \qquad (2)$$

$$\bar{E} = [\rho u, \rho u^2 + p, \rho uv, \rho uw, \rho uh]^t \qquad (3)$$

$$\bar{F} = [\rho v, \rho uv, \rho v^2 + p, \rho vw, \rho vh]^t \qquad (4)$$

$$\bar{G} = [\rho w, \rho uw, \rho vw, \rho w^2 + p, \rho wh]^t \qquad (5)$$

$$e = p/\rho(\gamma-1) + (u^2 + v^2 + w^2)/2 \qquad (6)$$

$$h = e + p/\rho \qquad (7)$$

● Rewriting the Equations in the Vector Form

$$\frac{\partial \rho}{\partial t} + \nabla \cdot (\rho \bar{V}) = 0 \qquad (8)$$

$$\frac{\partial(\rho\bar{V})}{\partial t} + \nabla \cdot (\rho \bar{V} \bar{V} + p \bar{\bar{I}}) = 0 \qquad (9)$$

$$\frac{\partial(\rho e)}{\partial t} + \nabla \cdot (\rho h \bar{V}) = 0 \qquad (10)$$

And Using the Substantial and Local Derivatives Relations

$$\frac{Da}{Dt} = \frac{D'a}{Dt} \; , \; \frac{\partial a}{\partial t} = \frac{\partial' a}{\partial t} + (\bar{V}_r - \bar{V}) \cdot \nabla a \tag{11}$$

$$\frac{D\bar{A}}{Dt} = \frac{D'\bar{A}}{Dt} + \bar{\omega}x\bar{A} \; , \; \frac{\partial \bar{A}}{\partial t} = \frac{\partial' \bar{A}}{\partial t} + (\bar{V}_r - \bar{V}) \cdot \nabla\bar{A} + \bar{\omega}x\bar{A} \tag{12}$$

where $\bar{V} = \bar{V}_r + \bar{\omega}x\bar{r}$; $\frac{D'}{Dt} , \frac{\partial'}{\partial t} \equiv$ Substantial and Local Derivative in the Rotating Frame

● We get the Conservative Form of Euler Equations for the Relative Motion

$$\frac{\partial' \rho}{\partial t} + \nabla \cdot (\rho \bar{V}_r) = 0 \tag{13}$$

$$\frac{\partial'(\rho \bar{V}_r)}{\partial t} + \nabla \cdot [\rho \bar{V}_r \bar{V}_r + p \bar{\bar{I}}] = - \rho[\dot{\bar{\omega}}x\bar{r} + 2\bar{\omega}xV_r + \bar{\omega}x(\bar{\omega}x\bar{r})] \tag{14}$$

$$\frac{\partial'(\rho e_r)}{\partial t} + \nabla \cdot [\rho h_r \bar{V}_r] = - \rho[V_r \cdot (\dot{\bar{\omega}}x\bar{r}) + (\bar{\omega}x\bar{r}) \cdot (\dot{\bar{\omega}}x\bar{r})] \tag{15}$$

where

$$e_r = \frac{P}{\rho(\gamma-1)} + \frac{V_r^2}{2} - \frac{1}{2} \left|\bar{\omega}x\bar{r}\right|^2 = e - \bar{V} \cdot (\bar{\omega}x\bar{r}) \tag{16}$$

$$h_r = \frac{\gamma p}{\rho(\gamma-1)} + \frac{V_r^2}{2} - \frac{1}{2} \left|\bar{\omega}x\bar{r}\right|^2 = h - \bar{V} \cdot (\bar{\omega}x\bar{r}) \tag{17}$$

Method of Solution

- The Abstract Conservative Form of the Relative Motion in Terms of Rotating Coordinates are

$$\frac{\partial'\bar{q}_r}{\partial t} + \frac{\partial'\bar{E}_r}{\partial x} + \frac{\partial'\bar{F}_r}{\partial y} + \frac{\partial'\bar{G}_r}{\partial z} = \bar{S} \tag{18}$$

where

$$\bar{q}_r = [\rho, \ \rho u_r, \ \rho v_r, \ \rho w_r, \ \rho e_r]^t \tag{19}$$

$$\bar{E}_r = [\rho u_r, \ \rho u_r^2 + p, \ \rho u_r v_r, \ \rho u_r w_r, \ \rho u_r h_r]^t \tag{20}$$

$$\bar{F}_r = [\rho v_r, \ \rho u_r v_r, \ \rho v_r^2 + p, \ \rho v_r w_r, \ \rho v_r h_r]^t \tag{21}$$

$$\bar{G}_r = [\rho w_r, \ \rho u_r w_r, \ \rho v_r w_r, \ \rho w_r^2 + p, \ \rho w_r h_r]^t \tag{22}$$

$$\bar{S} = [0, \ 0, \ \rho(\dot{\omega}z + 2\omega w_r + \omega^2 y), \ - \rho(\dot{\omega}y + 2\omega v_r - \omega^2 z), \ - \rho(-v_r \dot{\omega}z + w_r \dot{\omega}y + \dot{\omega}\omega y^2$$

$$+ \ \omega\dot{\omega}z^2)]^t \tag{23}$$

- The Source Term S has been Written for $\bar{\omega} = \omega \ \bar{e}_x$, $\dot{\bar{\omega}} = \dot{\omega} \ \bar{e}_x$

- Eqs. (18)-(23), (16) and (17) are Solved Using a Central-Difference, Finite-Volume Scheme Using Four-Stage Runge Kutta Time Stepping with Added Second- and Fourth-Order Dissipation Terms.

- The Computer Program is a Three-Dimensional Program.

• Local-Conical Flow Problem

- If the Conical Coordinates are Used to Transform the Relative Motion Equation, Eqs. (18)-(22), the Resulting Equations <u>will not</u> Represent a Conical Flow.

- If the Conical Coordinates are Used to Transform the Absolute Motion Equations, Eqs. (1)-(7), the Resulting Equations <u>will</u> Represent a Conical Flow for the Steady Flow. For the Unsteady Flow, the Problem is Made "Locally Conical" if it is Solved at a Fixed Axial Location.

- In the Three-Dimensional Program, Local Conical Flow Solutions are Obtained at x=1 by Equating the Absolute Motion in the First and Third Planes:

$$(\rho\bar{V})_{i\pm1} = (\rho\bar{V})_i \rightarrow (\rho\bar{V}_r)_{i\pm1} = (\rho\bar{V}_r) = (\rho\bar{V}_r)_i + \bar{\omega} \times (\rho_i\,\bar{r}_i - \rho_{i\pm1}\,\bar{r}_{i\pm1}) \tag{24}$$

$$(\rho E)_{i\pm1} = (\rho E)_i \rightarrow (\rho E_r)_{i\pm1} = (\rho E_r)_i + (\bar{V}_{ri} + \bar{\omega}\times\bar{r}_i) \cdot [\bar{\omega}\times(\rho_i\,\bar{r}_i - \rho_{i\pm1}\,\bar{r}_{i\pm1})] \tag{25}$$

where i = 2.

1. Initial Condition:

- For Constant Rolling Problem ($\bar{\omega} = -\omega_0 \, \bar{e}_x$), the Flow Corresponds to a Uniform Translation Plus a Rigid Body Rotation $-\bar{\omega} \times \bar{r}$.

- For Rolling Oscillation ($\bar{\omega} = -\omega_0 \sin kt \, \bar{e}_x$), the Flow Corresponds to a Uniform Translation Only.

2. Boundary Conditions:

- Normal Momentum Equation is Used on the Wing Surface
  $(\frac{D'}{Dt} (\bar{V}_r \cdot \hat{n}) = 0, \frac{\partial'\hat{n}}{\partial t} = 0)$

$$\rho \, \bar{V}_r \cdot (\bar{V}_r \cdot \nabla \hat{n}) = \frac{\partial P}{\partial n} + \rho \, \hat{n} \cdot [2\bar{\omega} \times \bar{V}_r + \dot{\bar{\omega}} \times \bar{r} + \bar{\omega} \times (\bar{\omega} \times \bar{r})] \qquad (26)$$

- In the Farfield, a Uniform Translation Plus the Corresponding Rotation are Imposed Outside of the Bow Shock.

SYMMETRIC CONICAL FLOW

This is a verification test case for the three-dimensional program which has been solved earlier by using a conical flow program[2]. Figure 2 shows the results for a flat plate sharp-edged delta wing at $M_\infty = 2$, $\alpha = 10^0$ and β (sweep angle) using a modified Joukowski transformation[2] of 128x64 cells around and normal to the wing has been used for the whole computational region. Figure 2 (a--d) shows the surface pressure, cross-flow velocity, cross-flow Mach contours and static pressure contours. It is clear that two symmetric leading-edge vortices have been captured on the suction side along with a weak cross-flow shock under each vortex. The outer bow shock is clearly visible in the lower portions of the cross-flow Mach and static pressure contours. The surface pressure, Mach contours and static-pressure contours match those obtained by using the conical flow program for half of the computational region.
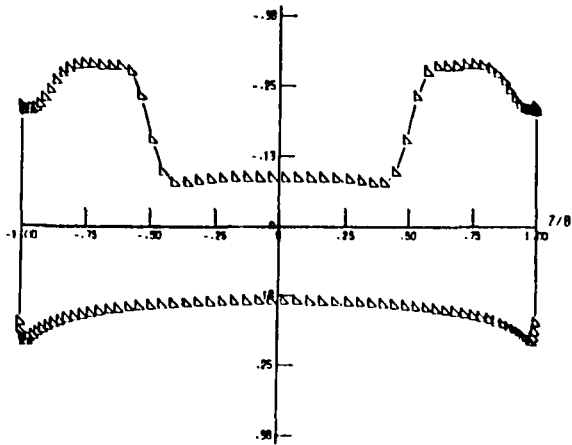
a. surface pressure
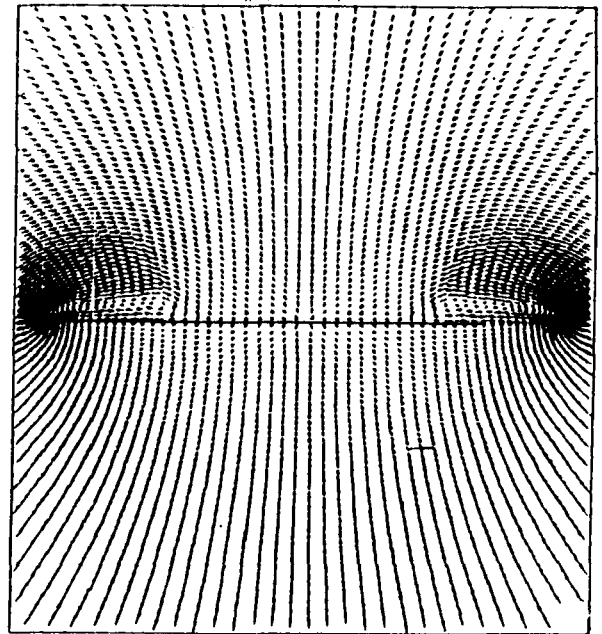
b. cross-flow velocity

Fig., 2 Steady symmetric flow around a delta wing, $M_\infty=2$, $\alpha=10^0$, $\beta=70^0$
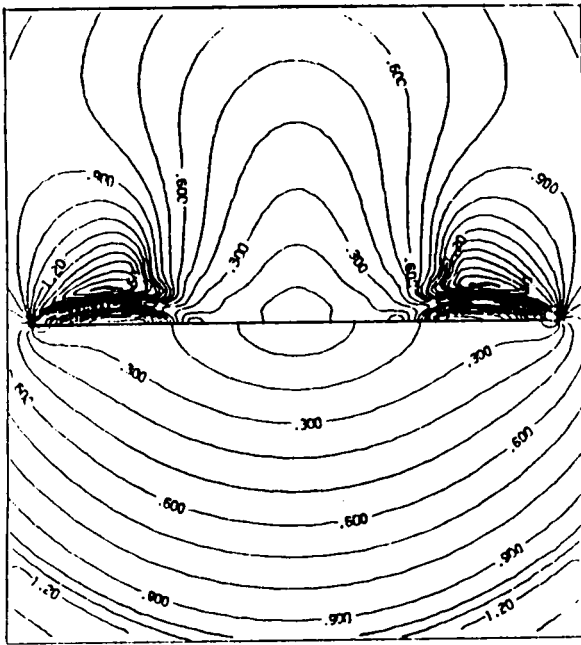
c. cross-flow Mach
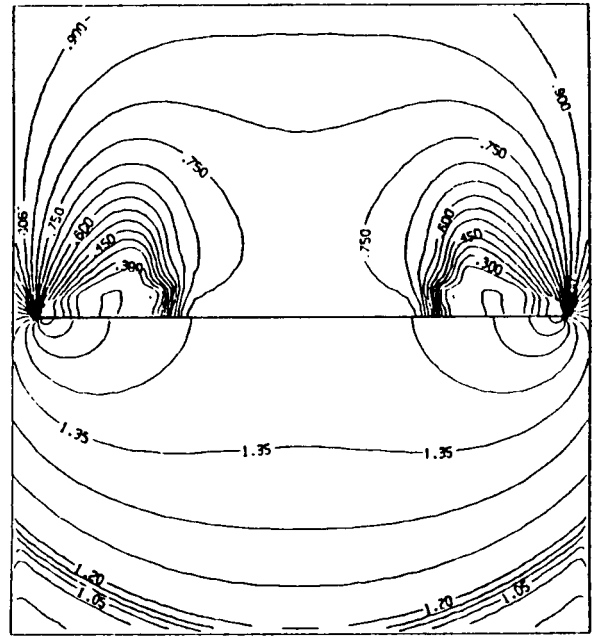
d. static pressure

Fig., 2 Steady symmetric flow around a delta
wing, $M_\infty=2$, $\alpha=10^0$, $\beta=70^0$

THREE-DIMENSIONAL TRANSONIC FLOW

Figure 3 shows the results of a sharp-edged delta wing for M_∞ = 0.7, α = 10° and aspect ratio of 1.5 using a number of cells of 80x38x48 in the x, η and ζ directions; respectively. The results of Figures 3a and 3b show, from left to right, the surface pressure, the static pressure contours and the cross-flow velocity; each at the chord stations of 0.52 and 0.81. Figure 3c shows the static pressure contours and the cross-flow velocity at the chord station of 1.01 and Figure 3a shows the static pressure contours and the cross-flow velocity at the chord station of 1.25. At x = 0.81, comparisons of the computed surface pressure with the experimental data[3] shows that the location of vortex core is well predicted, while the value of peak suction pressure under the vortex core is slightly underpredicted. At x = 1.25, the static pressure contours and the cross-flow velocity show the formation of trailing-edge vortex core and its interaction with the leading-edge vortex core. Our cross-flow planes are taken normal to the wing surface.
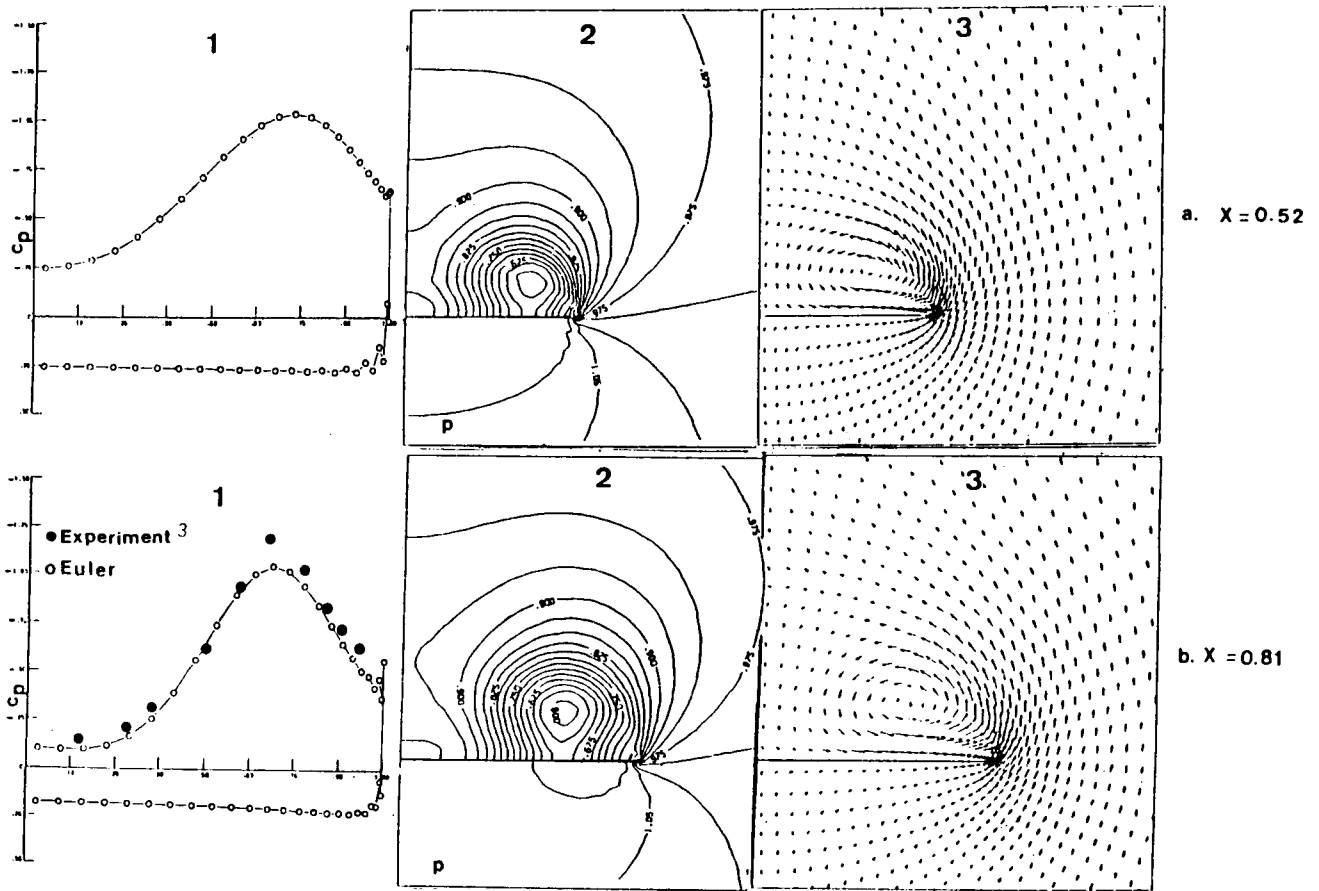
Figure 3 . Three-Dimensional Transonic Flow, Standard Euler Set, Sharp-edged delta wing, 80X38X48 cell, M_∞=0.7, α=15°, AR=1.5, ϵ_2=0.12, ϵ_4=0.005,
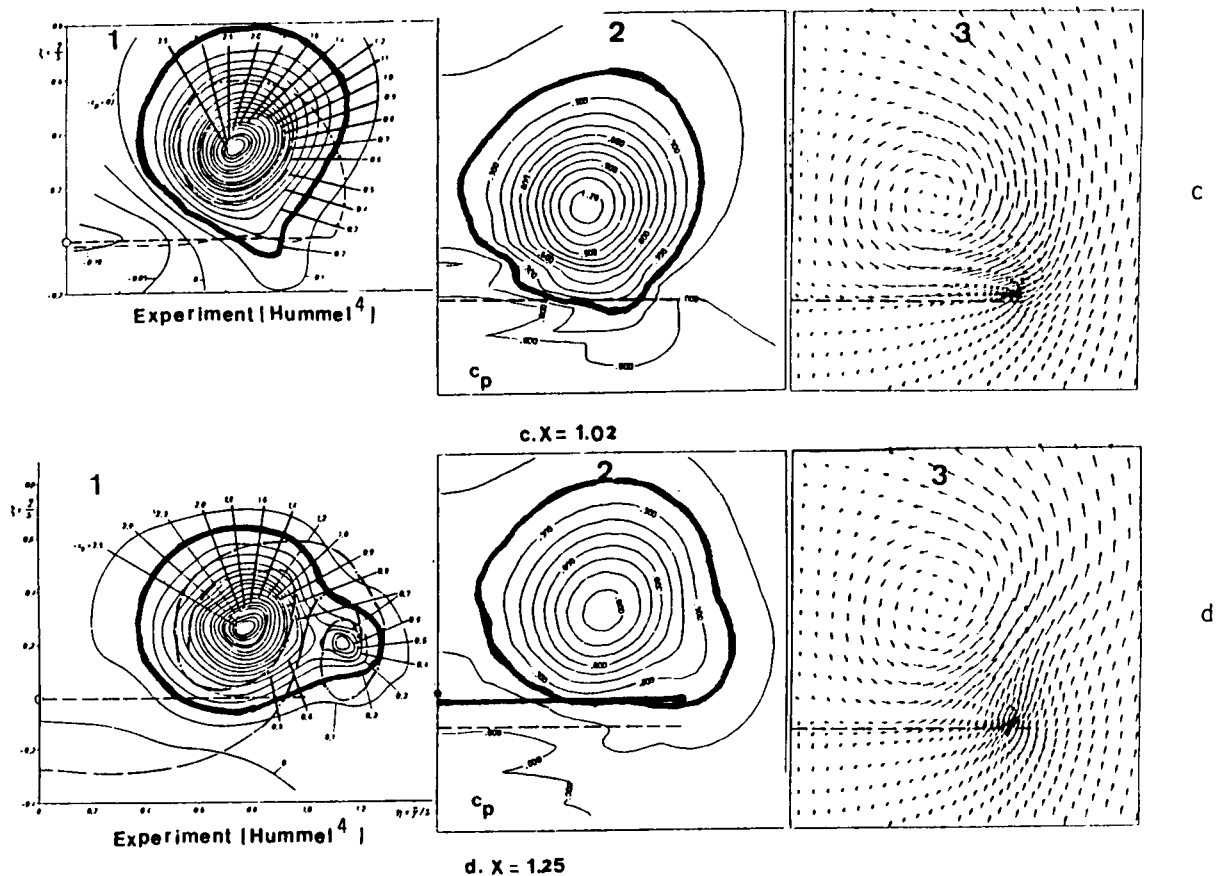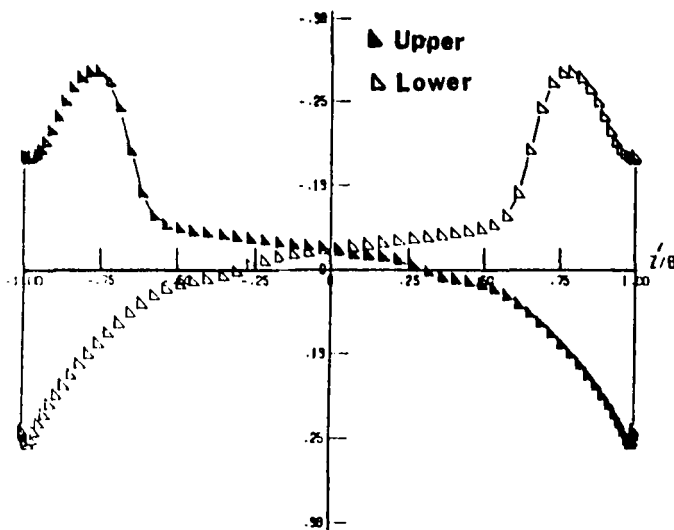(a.,b.)   1. Surface Pressure, 2. Static Pressure Contours, 3. Crossflow velocity
(c.,d.)1.Static pressure Contours, 2. Crossflow velocity
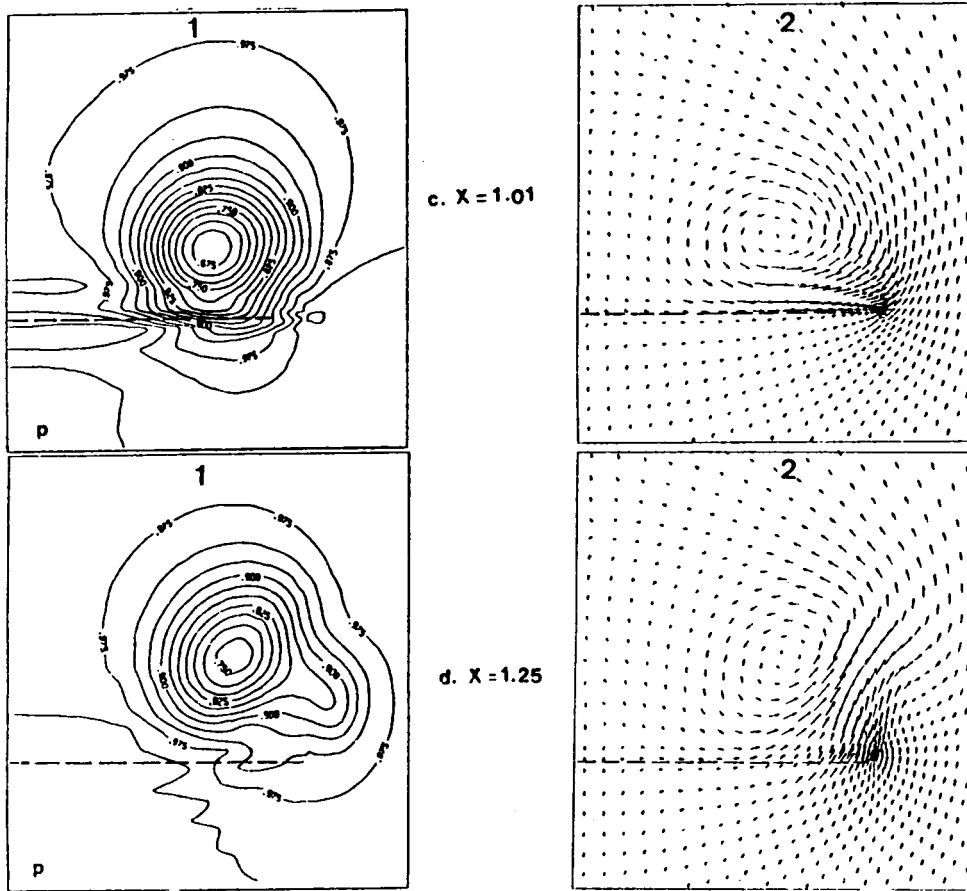
Figure 3 . Three-Dimensional Transonic Flow, Standard Euler Set, Sharp-edged delta
wing, 80X38X48 cell, M_=0.7, α=15⁰, AR=1.5, ϵ_2=0.12, ϵ_4=0.005,
(a., b.)   1. Surface Pressure, 2. Static Pressure Contours, 3. Crossflow
velocity
(c.,d.)1.Static pressure Contours, 2. Crossflow velocity

THREE-DIMENSIONAL LOW-SPEED FLOW

Figure 4 shows the results of a sharp-edged delta wing for M_∞ = 0.3, α = 20.5[0] and aspect ratio of 1 using a number of cells of 80x38x48 in the $\tilde{x}$, n, and ζ directions; respectively. The results of Figures 4a and 4b show, from left to right, the surface pressure and the experimental data of Hummel[4] the static-pressure-coefficient contours and the cross-flow velocity at the chord stations of 0.52 and 0.81. The results of Figures 4c and 4d show, from left to right, the experimental static-pressure-coefficient contours[4] (cross-flow planes are normal to wind direction), the computed static-pressure-coefficient (cross-flow planes are normal to wing surface) and the computed cross-flow velocity at the chord stations 1.02 and 1.25.

The results show that the location of leading-edge vortex core is accurately predicted, the suction pressure peak is accurately predicted at x = 0.52 but it is overpredicted at x = 0.81, the location of the trailing-edged vortex core is slightly off that of the experimental data. A finer grid than the one used in this example is expected to give a more accurate prediction.
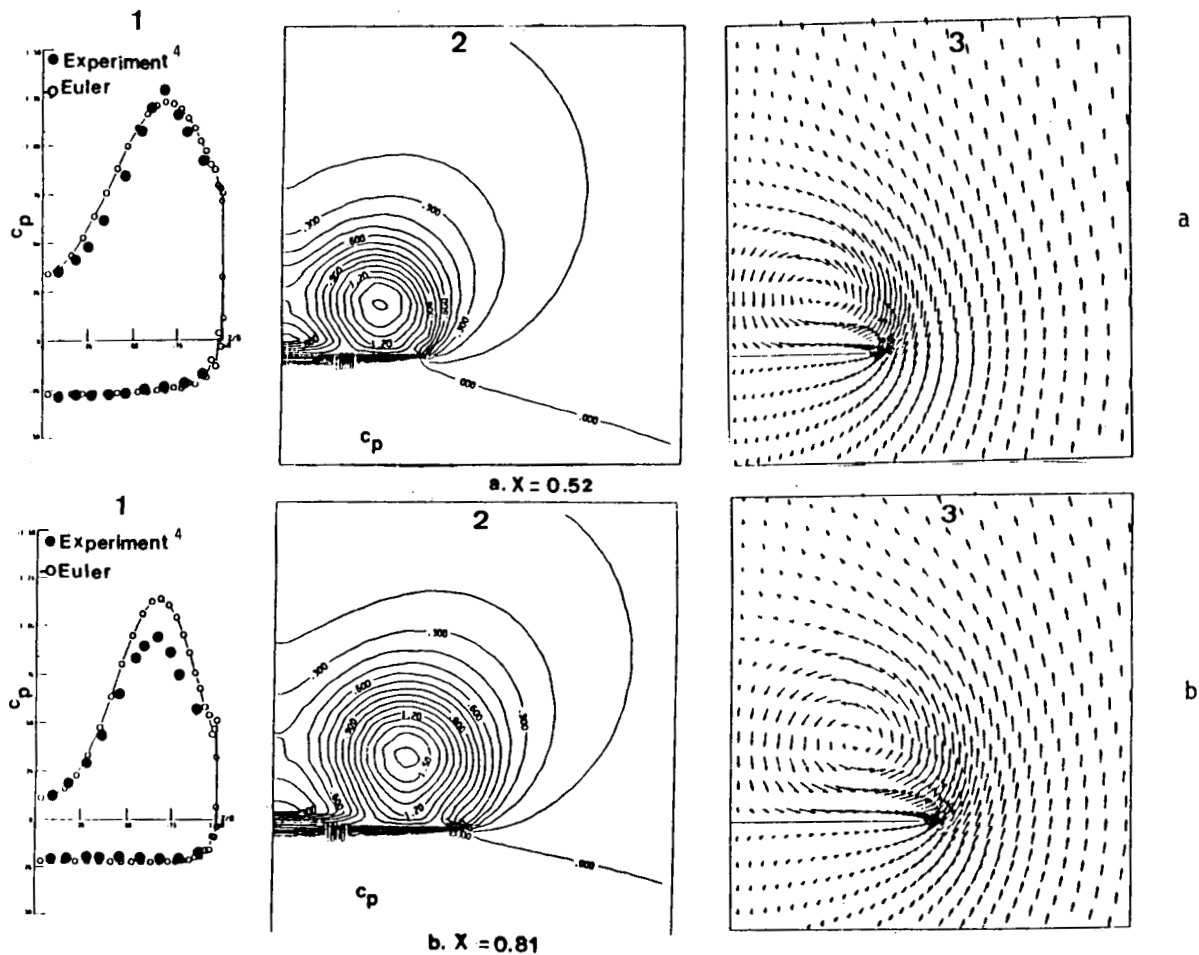
Figure 4. Three-dimensional subsonic flow, isentropic Euler set, sharp-edged delta wing, 80x38x48 cell, M_∞ = 0.3, α = 20.5°, AR = 1, ϵ_2 = 0.12, ϵ_4 = 0.005, (a.,b.) 1. surface pressure, 2. static presure contours, C_p, 3. crossflow velocity

Experiment (Hummel[4])

c. X = 1.02

Experiment (Hummel[4])

d. X = 1.25

Figure 4. Three-dimensional subsonic flow, isentropic Euler set, sharp-edged delta wing, 80x38x48 cell, $M_\infty = 0.3$, $\alpha = 20.5°$, AR = 1, $\epsilon_2 = 0.12$, $\epsilon_4 = 0.005$, (c.d.) 1. experimental static pressure contours, C_p, (normal to wind direction), 2. static pressure contours, C_p, (normal to wing surface), 3. crossflow velocity.

UNIFORM ROLLING IN A CONICAL FLOW

Figure 5 shows the results for a flat plate sharp-edged delta wing which is undergoing uniform rolling in the counter-clockwise direction around its axis ox' at a constant angular speed $\omega = \frac{\ell\omega^*}{U_\infty} = 0.5$; where ω^* and ω are the dimensional and dimensionaless angular speeds, ℓ is the wing root chord and U_∞ is the freestream speed. The wing angle of attack $\alpha = 0$ and hence the flow is steady in the rotating frame of reference. Figure 5a shows the upper "▲" and lower "△" surface pressure. As symmetric surface pressure. Figures 5b, 5c and 5d show the corresponding cross-flow velocity, cross-flow Mach contours an static pressure contours. On the cross-flow Mach contours and under the anti-symmetric leading-edge vortices, one notices a weak cross-flow shock.

a. surface pressure
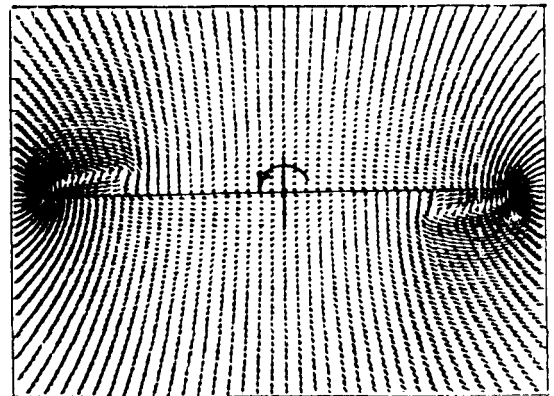
b. cross-flow velocity

Fig. 5 . Uniform rolling of a delta wing,
$M_\infty=2$, $\alpha=0^0$, $\beta=70^0$, $\omega=0.5$
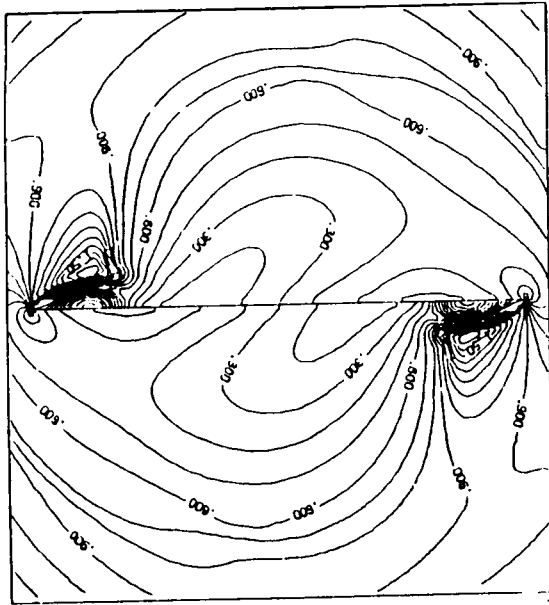
c. cross-flow Mach
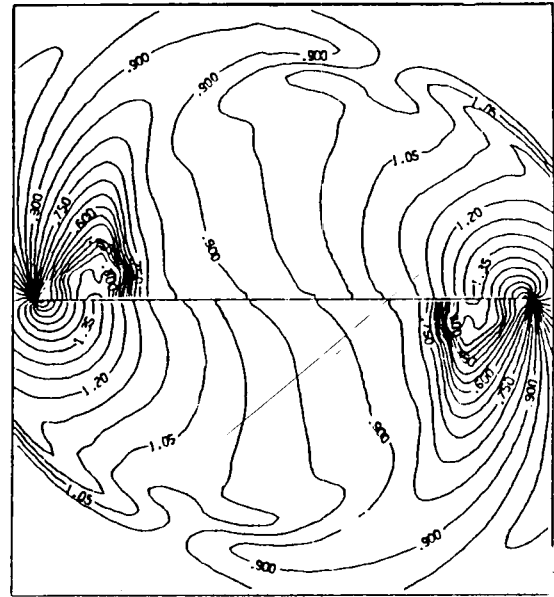
d. static pressure

Fig. 5. Uniform rolling of a delta wing,
$M_\infty=2$, $\alpha=0^0$, $\beta=70^0$, $\omega=0.5$

ROLLING OSCILLATION IN A LOCALLY-CONICAL FLOW

The wing is given a rolling sinusoidal oscillation of $\bar{\omega}$ and θ of $\bar{\omega} = -\omega_0 \cos kt$ $\hat{e}_x$, and $\theta = -\theta_{max} \sin kt$, where $\theta_{max} = \omega_0/k$ and k is the dimensionless reduced frequency of oscillation ($K = \frac{k \ell}{U}$ is the dimensional frequency). Choosing $\theta_{max} = \pi/12$ and $\omega_0 = 0.35$, the corresponding $k = 1.337$ and the period of oscillation $\tau = 4.699$. Figure 6 shows the rolling oscillation motion.

Point No.	Time	θ^0	Sense	Figure
1	1.07	-14.85	CCW	6
2	2.16	-3.76	CW	7
3	3.19	13.5	CW	8
4	4.31	7.46	CCW	9
5	5.35	-11.46	CCW	10
6	6.46	-10.63	CW	11
7	7.48	8.17	CW	12
8	8.59	13	CCW	13.1
9	9.69	-5.69	CCW	13.2
10	10.7	-14.79	CW	13.3
11	11.8	1.03	CW	13.4
12	12.8	14.8	CW	13.5
13	13.9	3.93	CCW	13.6
14	15.0	-14.01	CCW	13.7
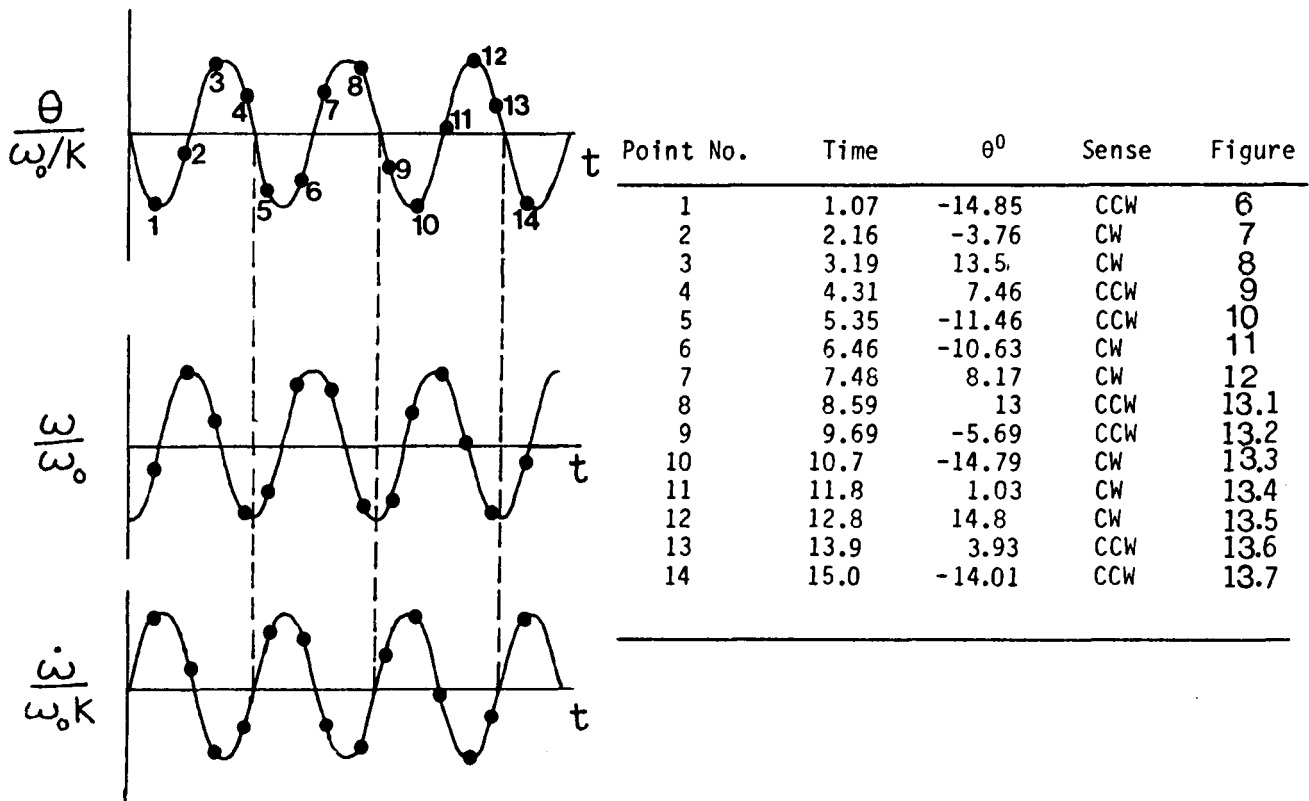
Fig. 6. Roll angle, angular speed and angular
acceleration of the rolling oscillation
motion.

Figure 7 shows the results for the time range t = 0 -1.07. By the end of this time, the wing has rolled through an angle θ = -14.85⁰ which corresponds to the end of the first quarter of the cycle. At t = 0, $|\omega|$ = ω_o and $|\omega|$ decreases in the counter-clockwise direction within that time. Figure 7a shows the surface pressure after each 400 time steps covering a total of 2000 time steps. On the upper surface, the suction pressure on the left is higher than that on the right, and the suction peak is moving in the spanwise direction in the positive z direction. On the lower surface, the surface pressure is decreasing on the left side while it is increasing on the right side. Figures 7b, 7c and 7d show the cross-flow velocity, cross-flow Mach contours and static pressure contours at t = 1.07 and θ = -14.85⁰. At this moment, a large leading-edge vortex appears on the left and a small leading-edge vortex appears on the right. The cross-flow Mach contours show shocks above and below the left leading-edge vortex. It also shows the outer bow shock with varying strength (lower portion of the figure).
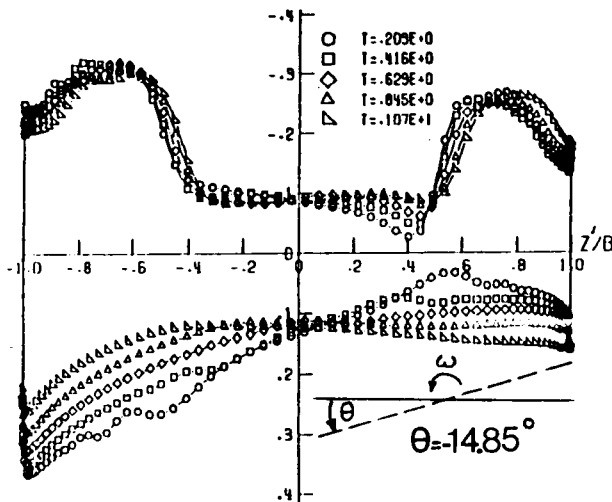

a. surface pressure
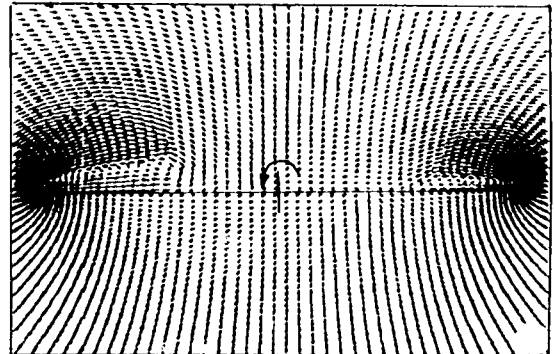

b. cross-flow velocity

Fig.7 . Rolling oscillation of a delta wing,
M_∞=2, α=10⁰, β=70⁰, ω=0.35, k=1.337,
θ_{max}=15⁰, t=0-1.07, θ=0-(-14.85⁰)
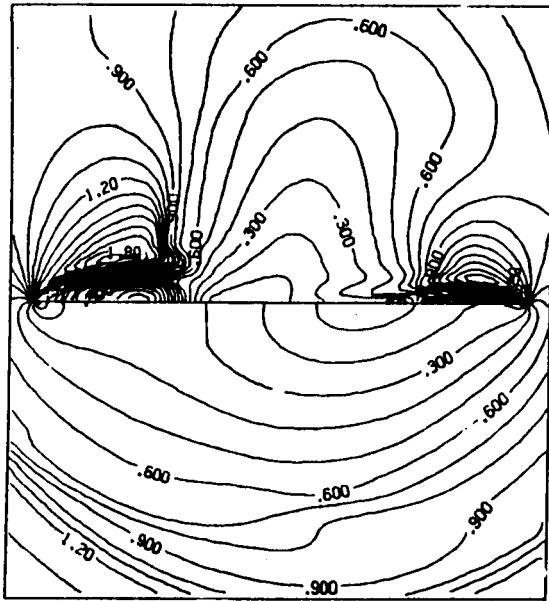
c. cross-flow Mach
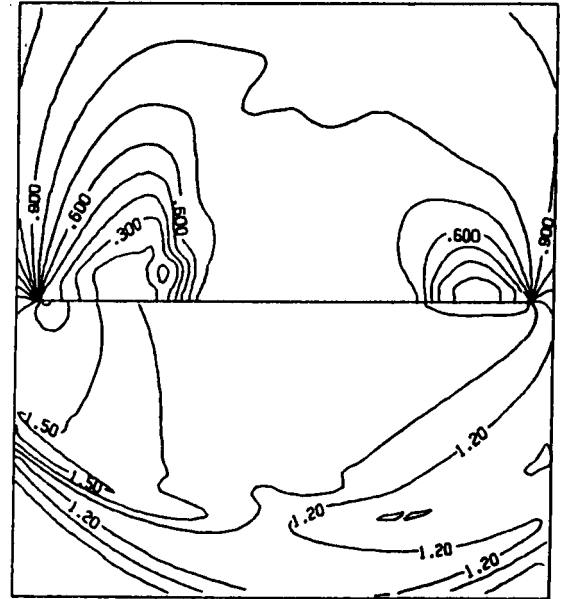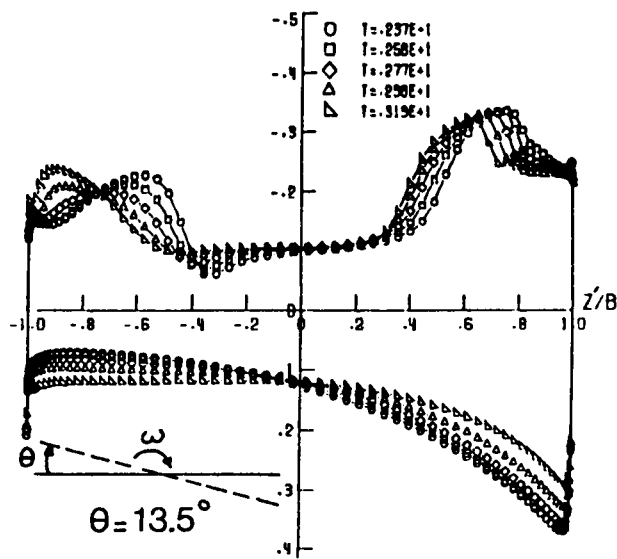
d. static pressure
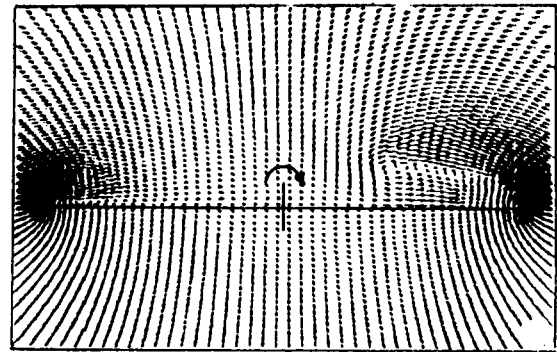
Fig. 7 . Rolling oscillation of a delta wing,
$M_\infty = 2$, $\alpha = 10^0$, $\beta = 70^0$, $\omega = 0.35$, $k = 1.337$,
$\theta_{max} = 15^0$, $t = 0-1.07$, $\theta = 0-(-1485^0)$

Figure 8 shows the results for the time range t = 1.07$^+$ - 2.16. Within this time, the wing has reversed it direction $|\omega|$, and by the end of this time, the wing roll angle θ = -3.76⁰. Figure 8a shows the surface pressure after each 400 time steps covering the range of time steps from 2,001-4,000. The peak suction pressure on the left is decreasing corresponding to a decrease in size of the left vortex while that on the right is increasing corresponding to an increase in size of the right vortex. Figures 8b, 8c and 8d show the cross-flow velocity, cross-flow Mach contours and static-pressure contours at t = 2.16, θ = -3.76⁰.
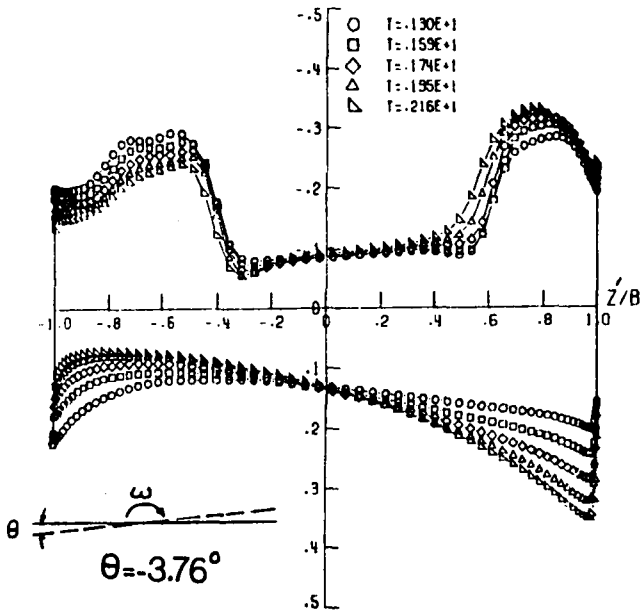

a. surface pressure
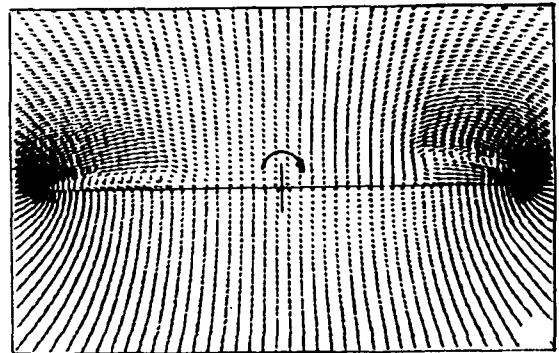
b. cross-flow velocity

Fig.8 . Rolling oscillation of a delta wing,
M_∞=2, α=10⁰, β=70⁰, ω=0.35, k=1.337,
$θ_{max}$=15⁰, t=1.07$^+$-2.16, θ=(-14.85⁰)-(-3.76⁰)
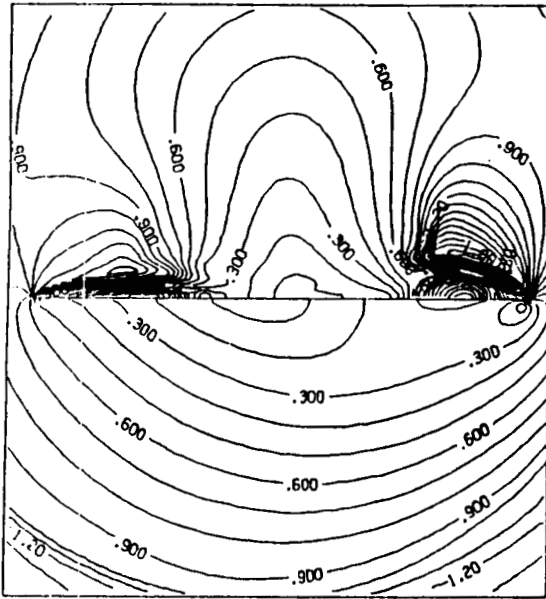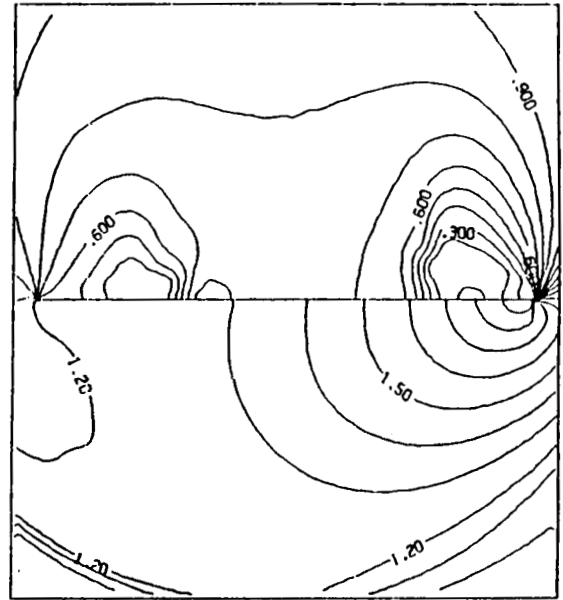
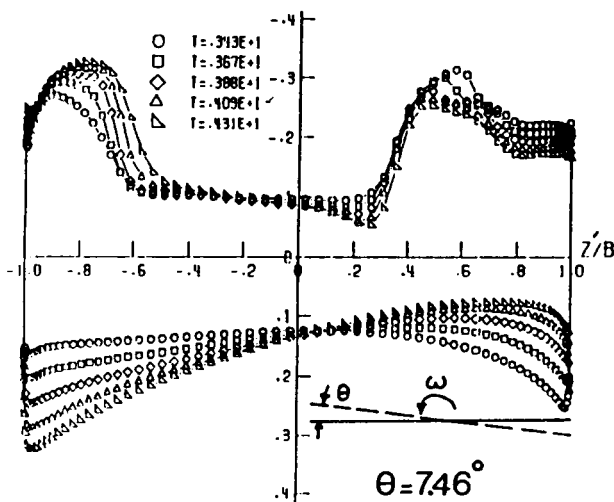c. cross-flow Mach   d. static pressure
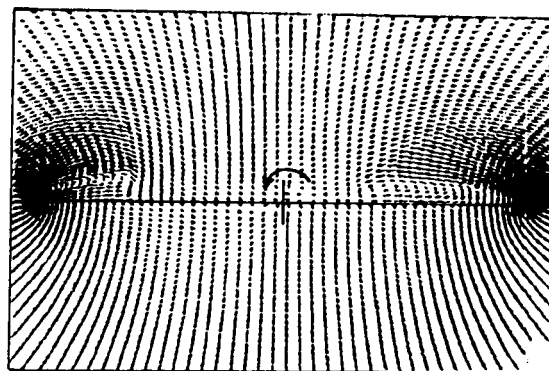
Fig.8 . Rolling oscillation of a delta wing,
     $M_\infty=2$, $\alpha=10^0$, $\beta=70^0$, $\omega=0.35$, $k=1.337$,
     $\theta_{max}=15^0$, $t=1.07^+-2.16$, $\theta=(-14.85^0)-$
     (-3.76^0)

Figure 9 shows the results for the time range $t = 2.16^+ - 3.19$ during which the wing is rotating in the clockwise direction with decreasing $|\omega|$. By the end of this time, the roll angle is $\theta = 13.5^0$. Figure 9a shows the surface pressure covering the range of time steps 4,001-6,000. The peak suction pressure on the left is moving to the left as the vortex is disappearing, and an attached flow is forming. Thepeak suction pressure on the right is moving inboards to the left, while the shock under the vortex is growing. Figures 9b, 9c and 9d show the cross-flow velocity, cross-flow Mach contours and static pressure contours at $t = 3.19$ and $\theta = 13.5^0$.

a. surface pressure   b. cross-flow velocity

Fig. 9. Rolling oscillation of a delta wing,
$M_\infty=2$, $\alpha=10^0$, $\beta=70^0$, $\omega=0.35$, $k=1.337$,
$\theta_{max}=15^0$, $t=2.16^+-3.19$, $\theta=(-3.76^0)-$
$(+13.6^0)$
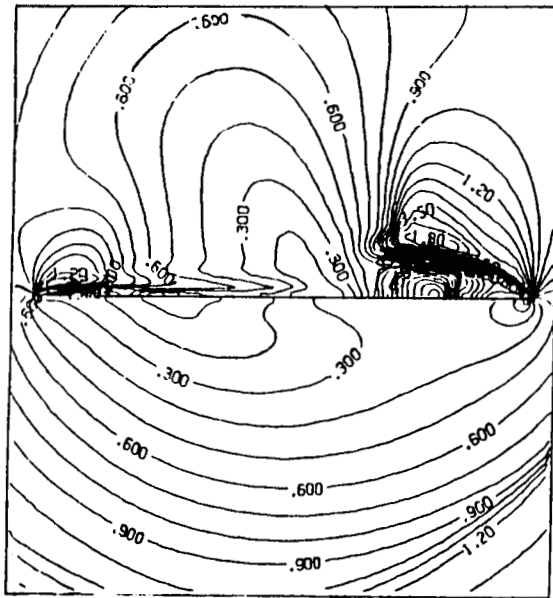
c. cross-flow Mach
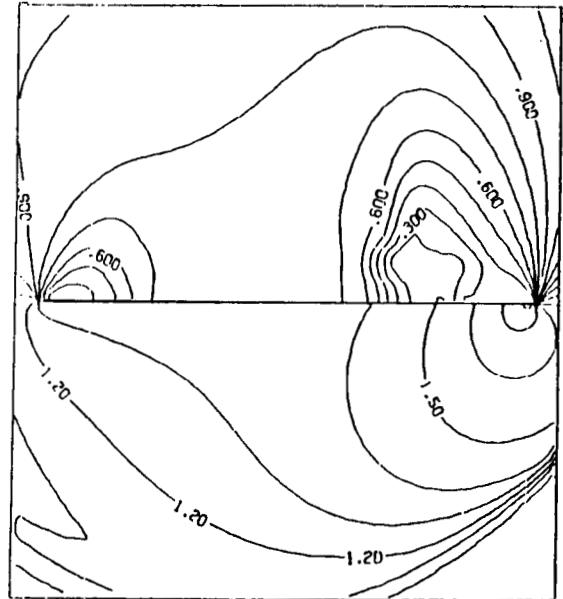
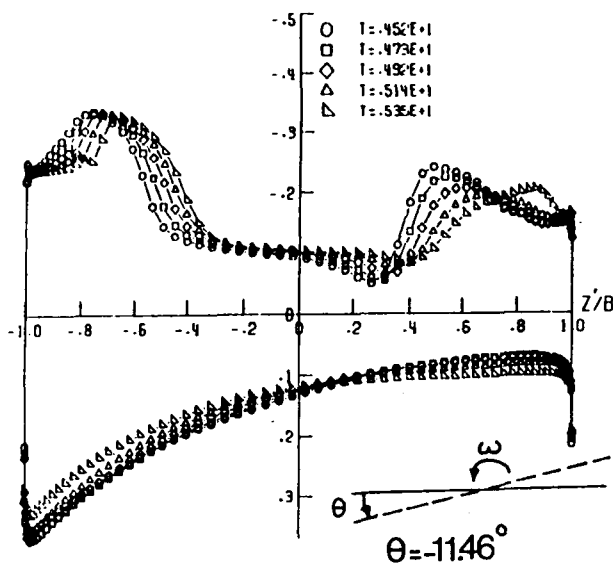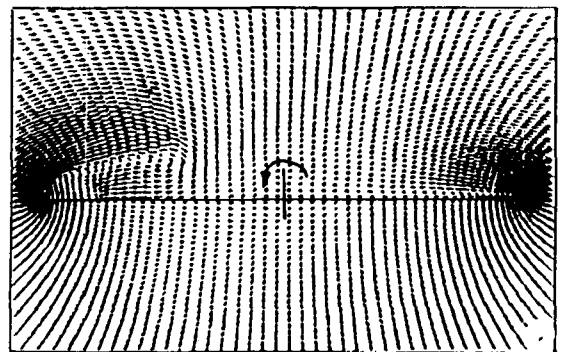d. static pressure

Fig. 9. Rolling oscillation of a delta wing,
$M_\infty=2$, $\alpha=10^0$, $\beta=70^0$, $\omega=0.35$, $k=1.337$,
$\theta_{max}=15^0$, $t=2.16^+-3.19$, $\theta=(-3.76^0)-$
$(+13.5^0)$

Figure.10(a-d) shows the results for the time range t = 3.19$^+$ - 4.31 during which the wing has reversed the direction of rotation from the CW to CCW, and $|\omega|$ has reached a zero value and then increases. The vortex on the left is growing, and the corresponding peak suction pressure is increasing and moving inboards to the right. The vortex on the right is flattening, and its peak suction pressure is decreasing and moving inboards to the left. By the end this time t = 4.31; the roll angle θ = 7.46°.


a. surface pressure

b. cross-flow velocity

Fig. 10. Rolling oscillation of a delta wing,
M_∞=2, α=10°, β=70°, ω=0.35, k=1.337,
θ_{max}=15°, t=3.19$^+$-4.31, θ=(+13.5°)- (+7.46°)
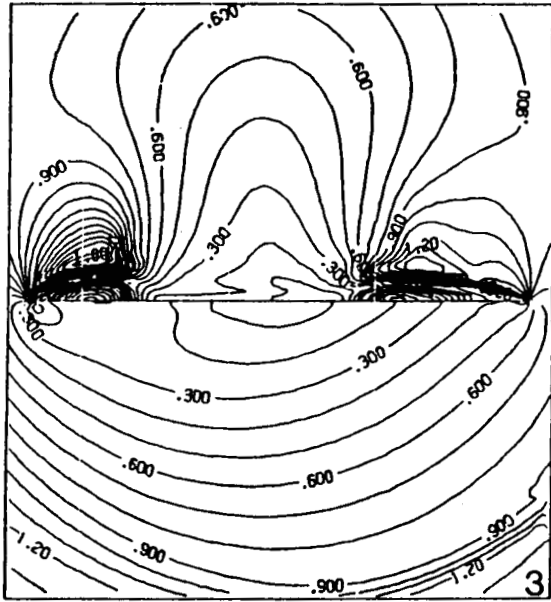
c. cross-flow Mach
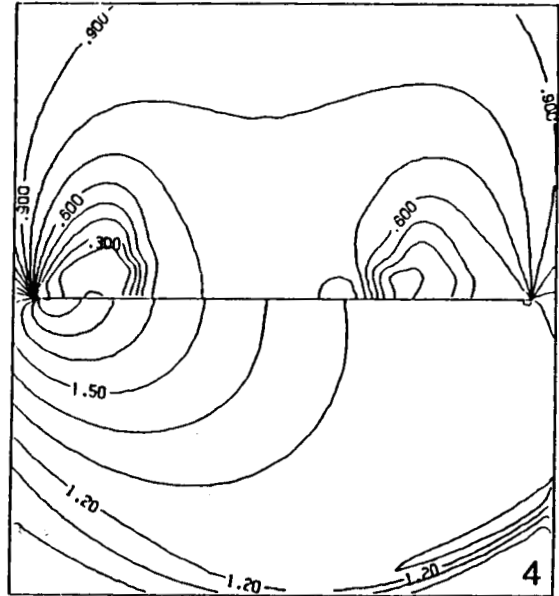
d. static pressure

Fig.10. Rolling oscillation of a delta wing,
$M_\infty=2$, $\alpha=10^0$, $\beta=70^0$, $\omega=0.35$, $k=1.337$,
$\theta_{max}=15^0$, $t=3.19^+-4.31$, $\theta=(+13.5^0)-$
$(+7.46^0)$

Within the time range $t = 4.31^+ - 5.35$, the wing is still rotating in the CCW, and $|\omega|$ has reached its maximum value and then decreases. At $t = 4.7$, the wing has already completed one cycle of oscillation. The peak suction pressure on the left is moving inboards to the right, and the peak suction pressure on the right is moving outboards to the right, Figure 11 (a--d). By the end of this time $t = 5.35$, the roll angle $\theta = -11.46^0$.

a. surface pressure

b. cross-flow velocity

Fig.11. Rolling oscillation of a delta wing,
$M_\infty = 2$, $\alpha = 10^0$, $\beta = 70^0$, $\omega = 0.35$, $k = 1.337$,
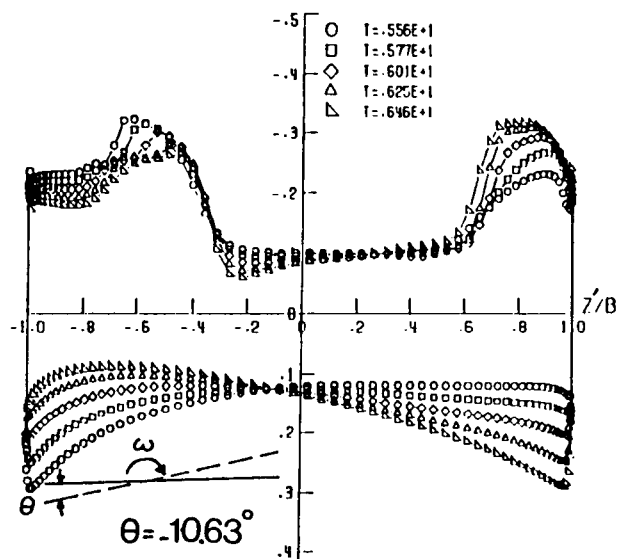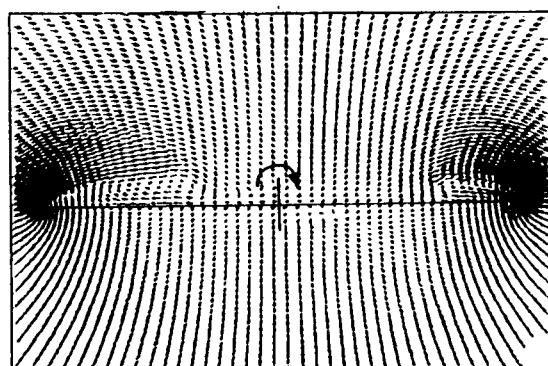$\theta_{max} = 15^0$, $t = 4.31^+ - 5.35$, $\theta = (+7.46^0) - (-11.46^\circ)$
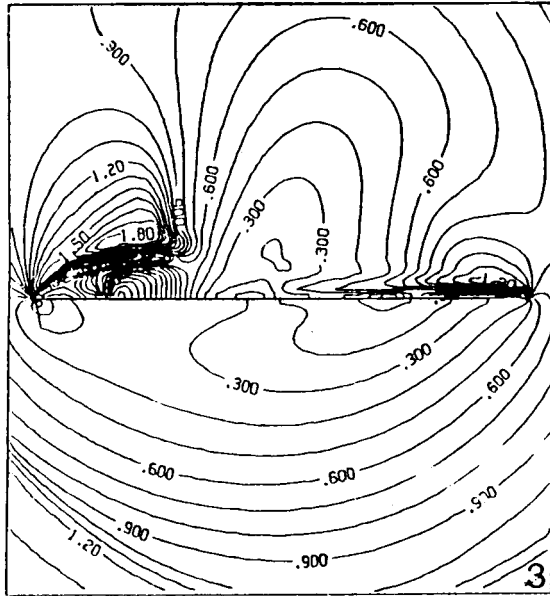
c. cross-flow Mach
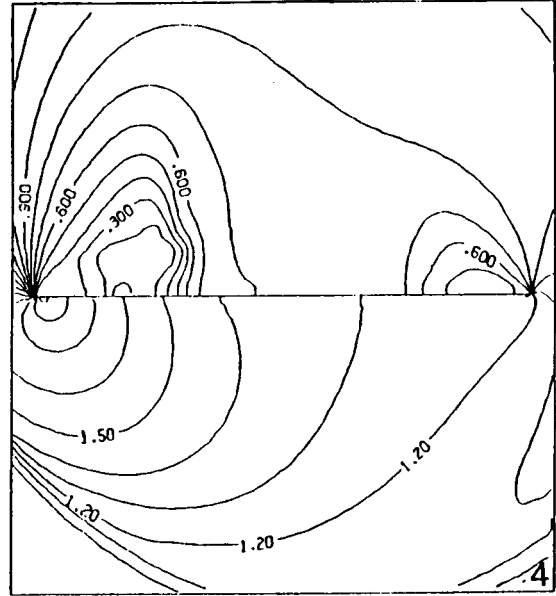
d. static pressure

Fig.11, Rolling oscillation of a delta wing,
$M_\infty = 2$, $\alpha = 10^0$, $\beta = 70^0$, $\omega = 0.35$, $k = 1.337$,
$\theta_{max} = 15^0$, $t = 4.31^+ - 5.35$, $\theta = (+7.45^0) - (-11.46°)$
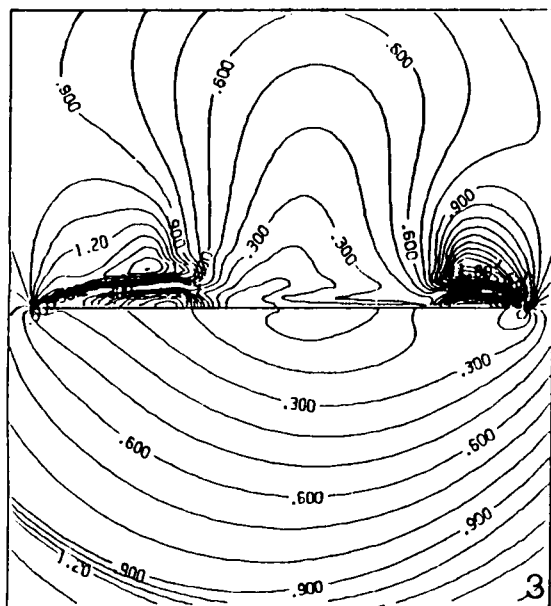
ROLLING OSCILLATION (CONTINUED)

Figures 12a-12d and 13a-13d show the results covering the ranges of time steps 10,001-12,000 and 12,001-14,000, respectively. Figures 5-11 cover a total of 1.56 cycles of oscillation. The results show the successive increase, decreased and motion of the left and right vortices and their corresponding peak suction pressure. They also show the formation and disintegration of the shocks below and above the vortices, and the motion and strength variation of the outer bow shock.
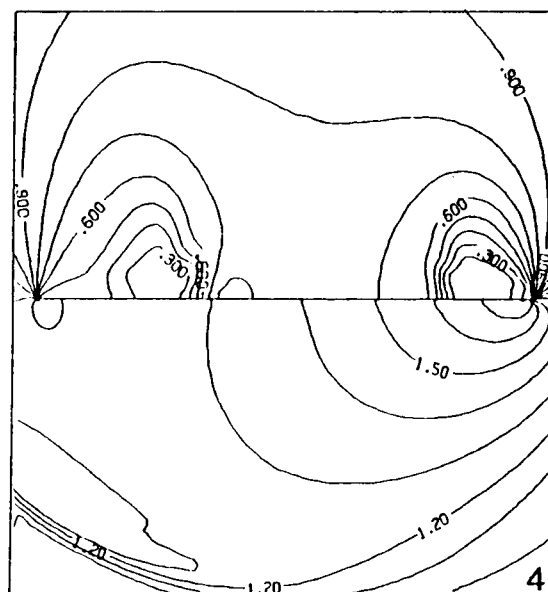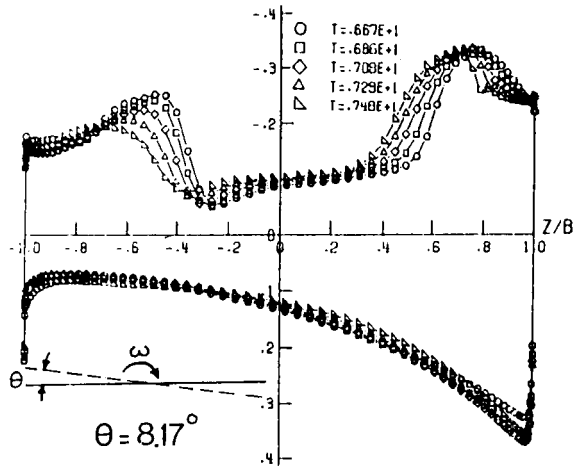

a. surface pressure
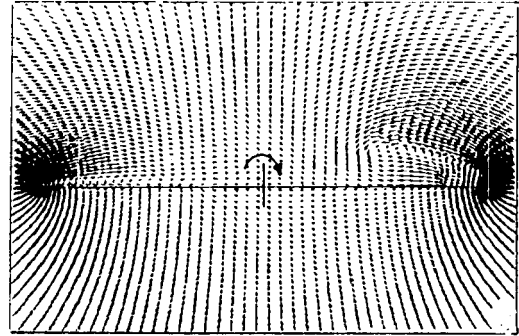

b. cross-flow velocity

c. cross-flow Mach

d. static pressure

Fig. 12. Rolling oscillation of a delta wing,
$M_\infty=2$, $\alpha=10^0$, $\beta=70^0$, $\omega=0.35$, $k=1.337$,
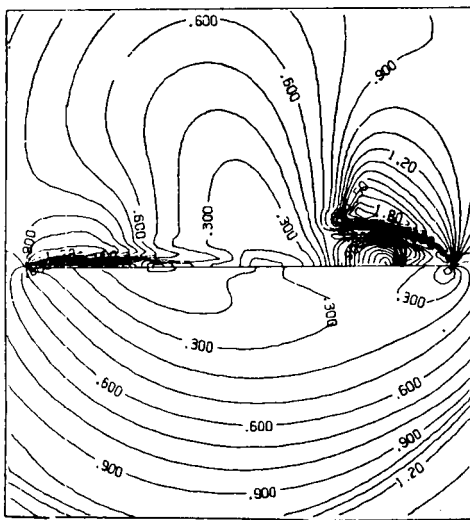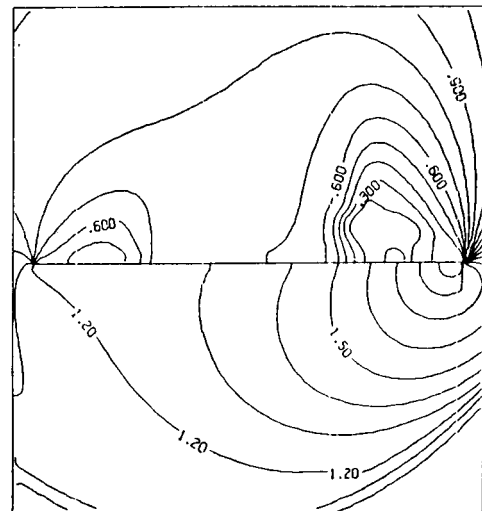$\theta_{max}=15^0$, $t=5.35^+$-6.46, $\theta=(-11.46^0)-(-10.63^0)$

288

a. surface pressure

b. cross-flow velocity

c. cross-flow Mach

d. static pressure

Fig. 13. Rolling oscillation of a delta wing,
$M_\infty = 2$, $\alpha = 10^0$, $\beta = 70^0$, $\omega = 0.35$, $k = 1.337$,
$\theta_{max} = 15^0$, $t = 6.46^+ - 7.48$, $\theta = (10.63^0) - (+8.17^\circ)$

ROLLING OSCILLATION (CONCLUDED)

Steady state oscillation response is reached after 3 cycles of transient response, Figure 14 (a--g).
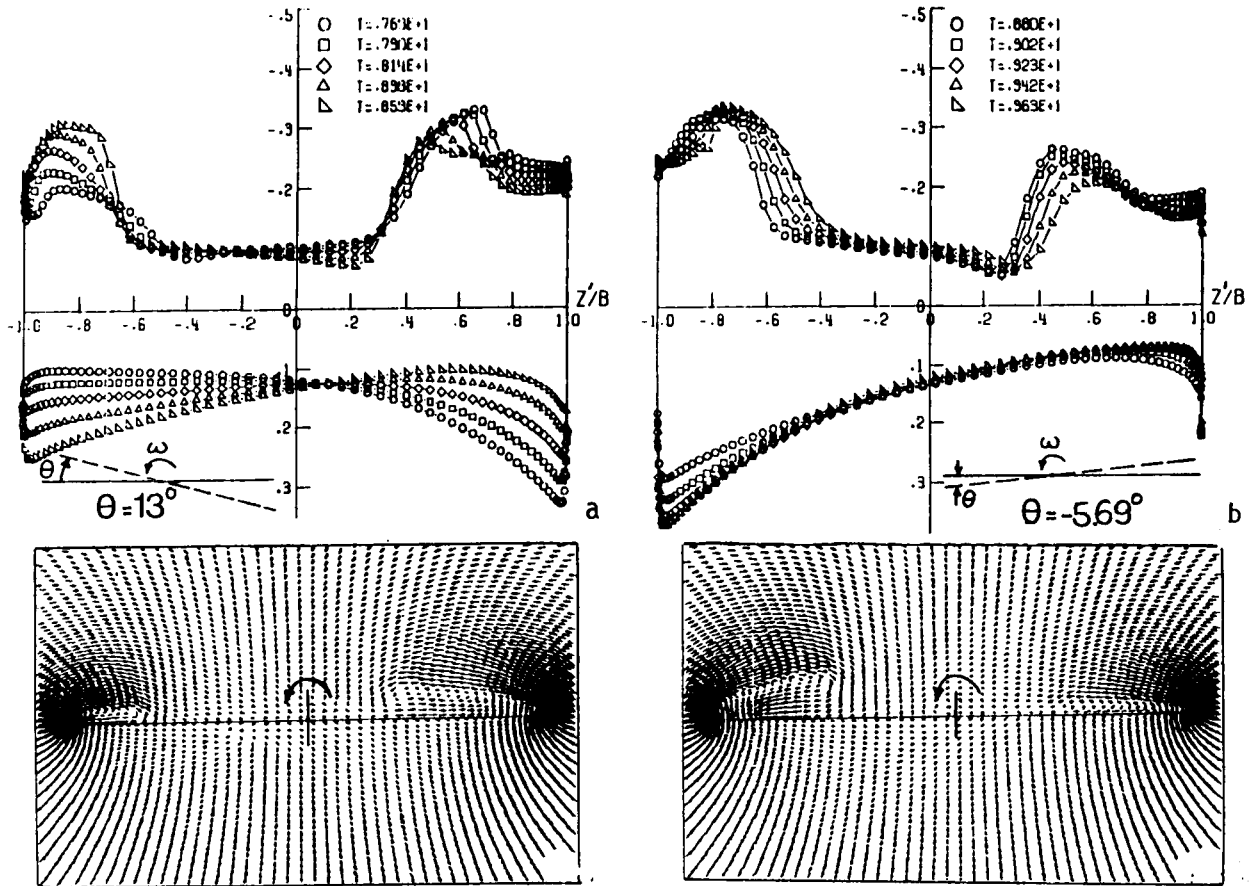

Fig. 14 . Rolling oscillations from t = 7.48[+]
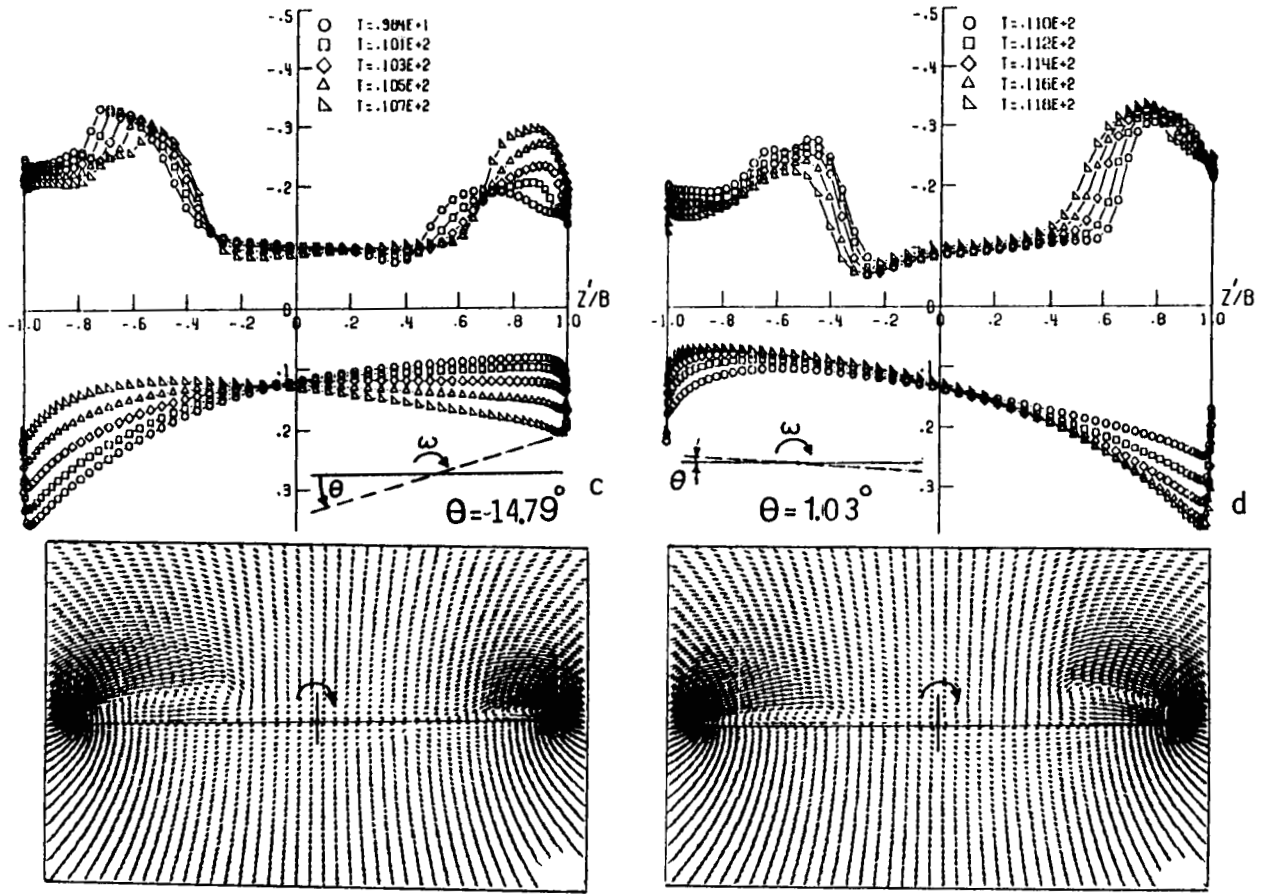to t = 15.0, steady state oscilla-
tion is reached.

Fig. 14. Continued.
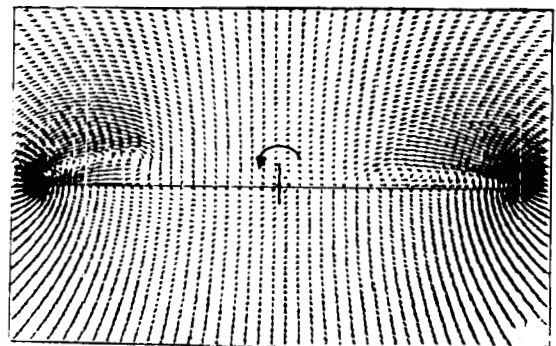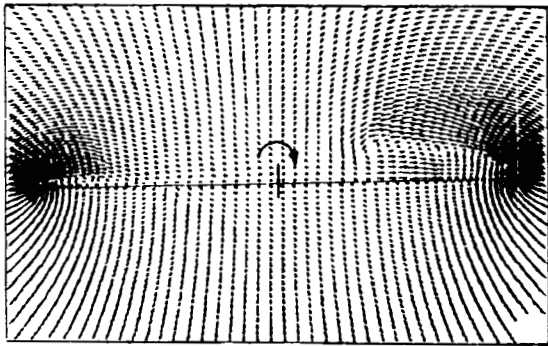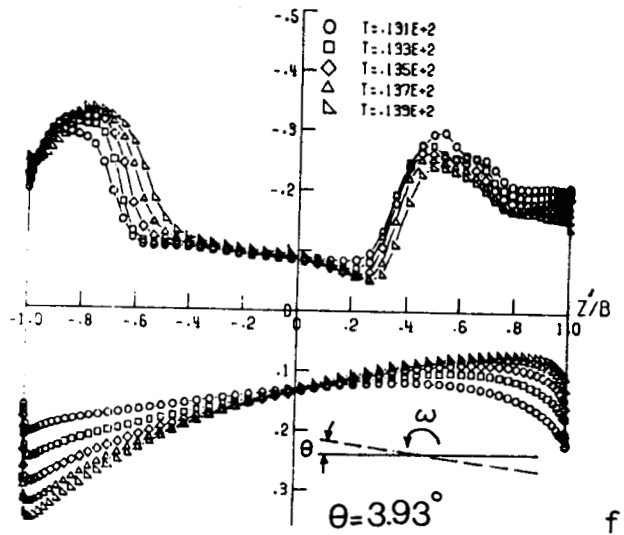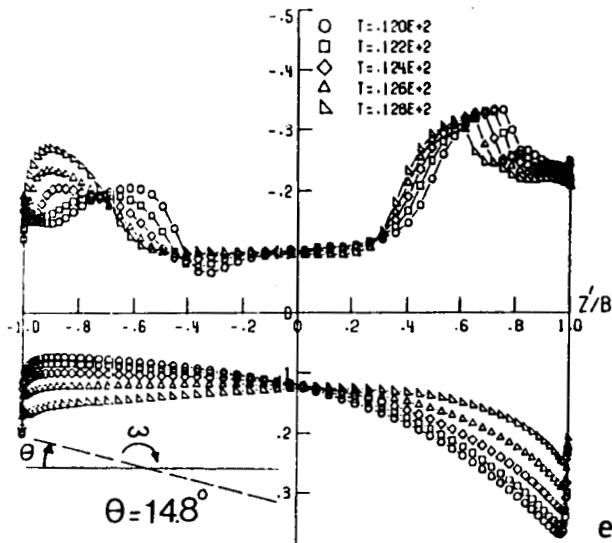
Fig. 14. Continued.
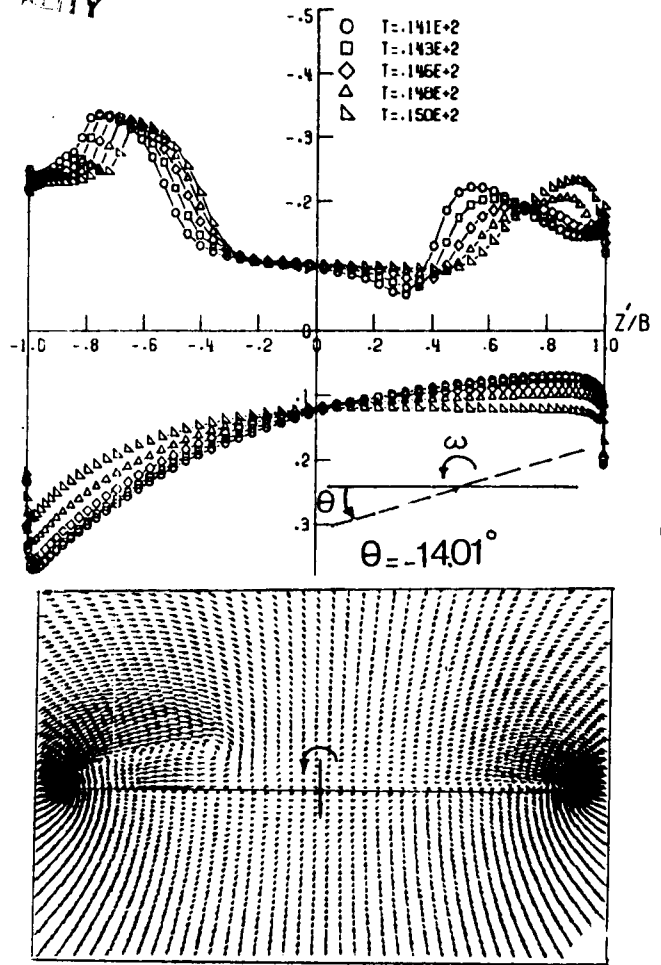
Fig. 14. Concluded.

ROLLING OSCILLATION, LIFT AND ROLLING-MOMENT COEFFICIENTS

Figure 15 shows the time history of the lift and rolling-moment coefficients along with roll angle variation. Steady-state oscillation response is reached by the third cycle. While the phase angle between C_M and θ is 90°, C_M is in phase with ω. Although C_M and θ have the same frequency, C_L shows twice the value of that frequency.

FIGURE 15. TIME HISTORY OF THE LIFT AND ROLLING-MOMENT COEFFICIENTS

294

3. Integral Solution of Full-Potential Equation With and Without Embedded Euler Domains

Formulation

Full Potential Equation (Shock Capturing, SC; Shock Capturing-Shock Fitting, SCSF)

$$\Phi_{xx} + \Phi_{yy} = G \tag{1}$$

$$G = \frac{-1}{\rho} (\rho_x \Phi_x + \rho_y \Phi_y) \tag{2}$$

$$\rho = [1 + \frac{\gamma-1}{2} M_\infty^2 (1 - \Phi_x^2 - \Phi_y^2)]^{1/\gamma-1} \tag{3}$$

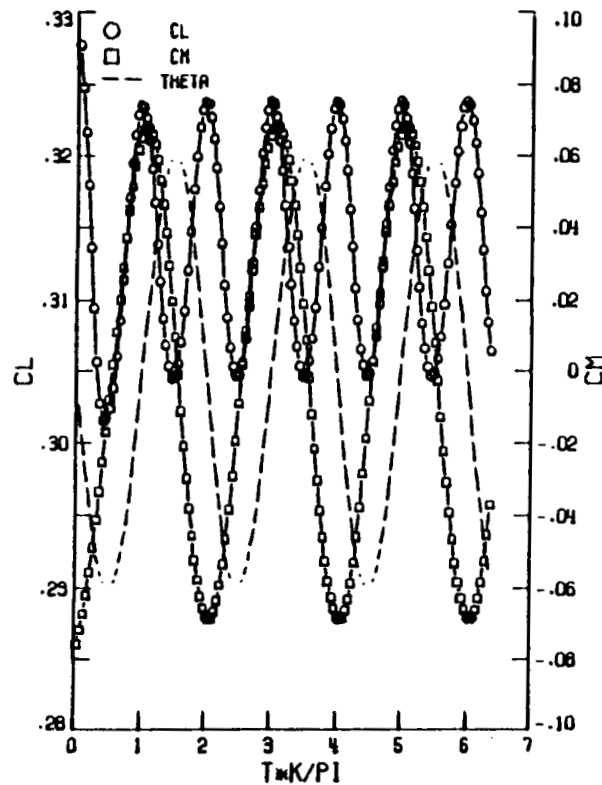$$\nabla\Phi \cdot \hat{n} = 0 \qquad \text{on } g(x, y) = 0 \tag{4}$$

$$\nabla\Phi \rightarrow \bar{e}_\infty \qquad \text{away from } g \tag{5}$$

$$\Delta C_p\big|_{TE} = 0 \tag{6}$$

Integral Solution of Velocity Field With Explicit Shock Surface Contribution

$$\nabla\Phi(x,y) = \bar{e}_\infty + \frac{1}{2\pi} \oint_g q_g(s) \frac{(x-\xi) \bar{i} + (y-\eta) \bar{j}}{(x-\xi)^2 + (y-\eta)^2} ds$$

$$+ \frac{1}{2\pi} \oint_g \gamma_g(s) \frac{(y-\eta) \bar{i} - (x-\xi) \bar{j}}{(x-\xi)^2 + (y-\eta)^2} ds$$

$$+ \frac{1}{2\pi} \iint G(\xi,\eta) \frac{(x-\xi) \bar{i} + (y-\eta) \bar{j}}{(x-\xi)^2 + (y-\eta)^2} d\xi d\eta$$

$$+ \frac{1}{2\pi} \oint_S q_S(s) \frac{(x-\xi) \bar{i} + (y-\eta) \bar{j}}{(x-\xi)^2 + (y-\eta)^2} ds \tag{7}$$

Shock Fitting

$$q_S = - (V_{1n} - V_{2n}) = - \frac{2 V_{1n}}{\gamma+1} (1 - \frac{1}{M_{1n}^2}) \quad , M_{1n} > 1 \tag{8}$$

$$V_{2n} = \frac{(\gamma-1) M_{1n}^2 + 2}{(\gamma+1) M_{1n}^2} V_{1n} \tag{9}$$

$$V_{2t} = V_{1t} \tag{10}$$

$$\rho_2 = \frac{(\gamma+1) M_{1n}^2}{(\gamma-1) M_{1n}^2 + 2} \rho_1 \tag{11}$$

$$\beta = \sin^{-1} [\frac{1.2 \sin\beta \sin\theta}{\cos (\beta-\theta)} + \frac{1}{M_1^2}]^{1/2} \tag{12}$$

$$M_1 = M_\infty |\nabla\Phi|_1 / \rho_1^{\frac{\gamma-1}{2}} , \quad M_{1n} = M_\infty \nabla\Phi_1 \cdot \hat{n}_S / \rho_1^{\frac{\gamma-1}{2}} \tag{13}$$

Pressure Coefficient

$$C_p = \frac{2}{\gamma M_\infty^2} \{[1 + \frac{\gamma-1}{2} M_\infty^2 (1 - \Phi_x^2 - \Phi_y^2)]^{\gamma/\gamma-1} - 1\} \tag{14}$$

Euler Equations (Integral Equation With Embedded Euler Domains)

$$\frac{\partial \bar{q}}{\partial t} + \frac{\partial \bar{E}}{\partial x} + \frac{\partial \bar{F}}{\partial y} = 0 \qquad (15)$$

$$\bar{q} = [\rho, \ \rho u, \ \rho v, \ \rho e]^t \qquad (16)$$

$$\bar{E} = [\rho u, \ \rho u^2 + p, \ \rho uv, \ \rho uh]^t \qquad (17)$$

$$\bar{F} = [\rho v, \ \rho uv, \ \rho v^2 + p, \ \rho vh]^t \qquad (18)$$

$$e = \frac{p}{(\gamma+1)\rho} + (u^2 + v^2)/2, \quad h = e + p/\rho \qquad (19)$$

Method of Solution

- **Shock-Capturing Shock-Fitting (SCF) Scheme:**

  - **Shock Capturing Part**

  1. In Eq. (7), Set $G = q_s = 0$, Use Eq. (7) to Satisfy B.C.S; Eqs. (4), (6). Find q_g and γ_g (piecewise linear distribution).

  2. Calculate Initial Values of G at the Centroids of Field Elements ($G = M_\infty^2 u_x$).

  3. With $q_s = 0$, Eq. (7) is Used to Satisfy B.C.S.

  4. Calculate ρ and G Using Eqs. (2), (3) (Type Finite Difference is Used for ρ_x, ρ_y).

  5. Steps (3) and (4) are Repeated Until Captured Shock Location is Fixed.

  - **Shock Fitting Part**

  6. Shock Panels are Introduced, q_s - term in Eq. (7) is activated.

  7. Eqs. (8) and (12) are Used to Find q_s and β, and Eqs. (9)-(12) are Used to Cross the Shock.

  8. Iterative Procedure is Continued Until Convergence.

● Integral Equation With Embedded Euler (IEEE) Scheme (For Strong Shocks)

1. Shock Capturing is Used to Locate the Shock.

2. A Computational Fine-Grid Domain is Constructed Around the Shock for Euler Computations.

3. With B.C. and I.C. Found From Step (1), Euler Eqs. (15)-(19) are solved by Using a Central-Difference Finite-Volume Solver with Four-Stage Runge-Kutta Time Stepping and Added Second- and Fourth-Order Dissipation.

4. Fixing $\bar{q}$ Values Found From the Euler Calculations, the Integral Eq. is Used to Update the B.C.

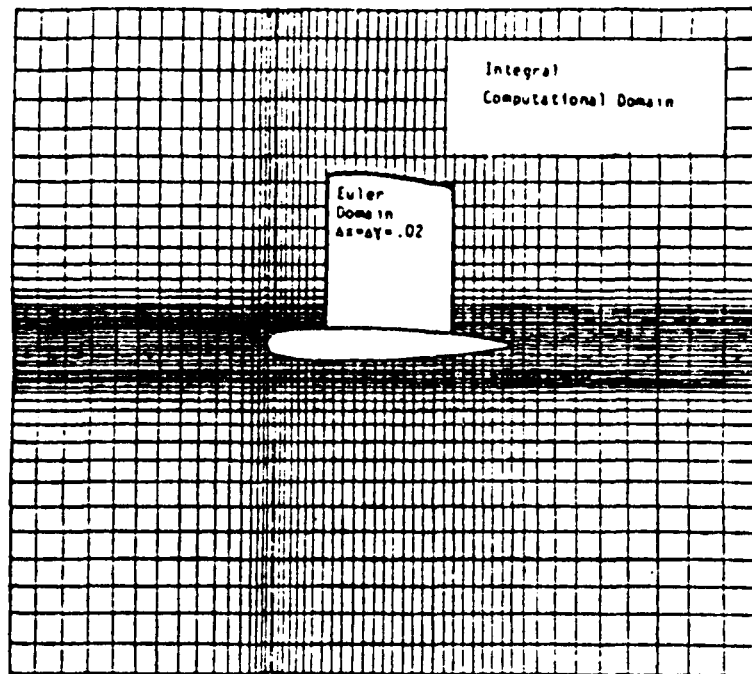5. The Iterative Procedure is Continued Until Convergence is Achieved.

Fig.16   Integral Equation Grid with an
          Embedded-Euler Domain.

The first step to validate the computer program is to check the sensitivity of the IE solution to the size of the computational domain. Figure 17 shows the solutions for the NACA 0012 airfoil at $M_\infty = 0.72$ and $\alpha = 0^0$ using vortex panels only on the airfoil surface. We used a total of 140 vortex panels on the airfoil surface and a 64x60 field elements around the airfoil. The solutions show the surface pressure using two sizes of the computational domains; 2x1.5 and 3x2.5. In Figure 18, we repeat the same test for a lifting case of the same airfoil at $M_\infty = 0.63$ and $\alpha = 2^0$. The results of these two cases show that a computational domain of 2x1.5 gives as accurate solutions as those of the 3x2.5 computational domain.
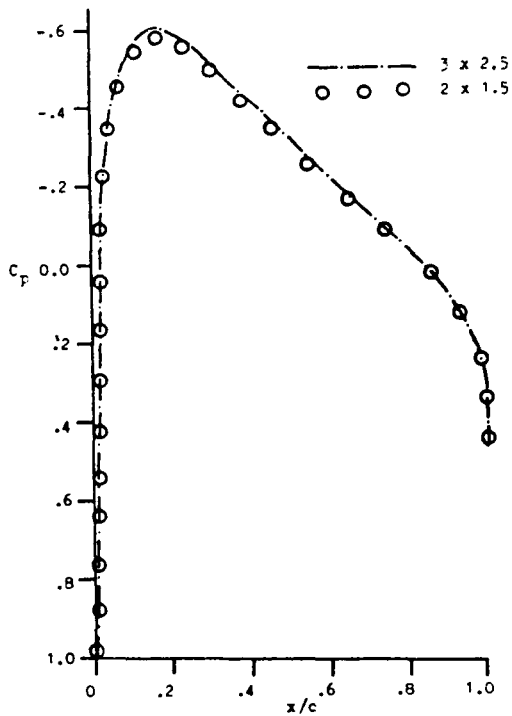

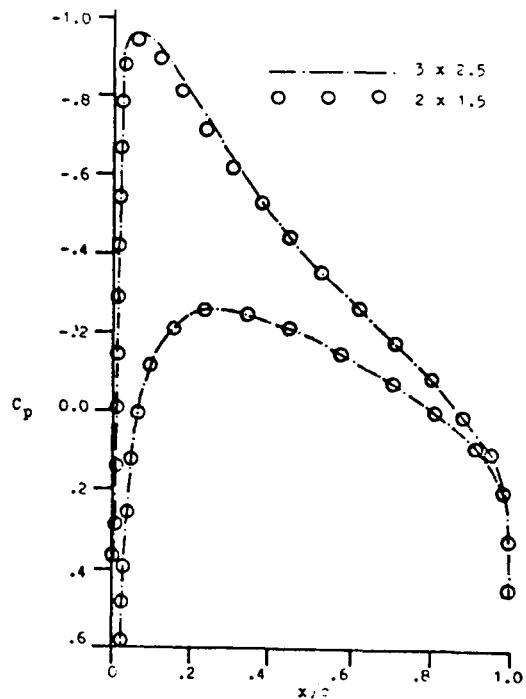Fig. 17   Effect of the Computational Domain Size, Surface Vortex Panels, NACA 0012, M_∞=0.72, α=0^0.

Fig. 18   Effect of the Computational Domain Size, Surface Vortex Panels, NACA 0012, M_∞=0.63, α=2^0.

The second numerical test is aimed at comparing the results of the IE solution using vortex panels only and source panels only with the solution of Euler equations[5]. Figure 19 shows the results of this test for the NACA 0012 airfoil at $M_\infty = 0.7$ and $\alpha = 0^0$. The computational domain is 2x1.5, and the same numbers of surface panels and field elements as those of Figure 17 have been used. It is clear that the IE solution with surface vortex panels is superior to that of the source panels.
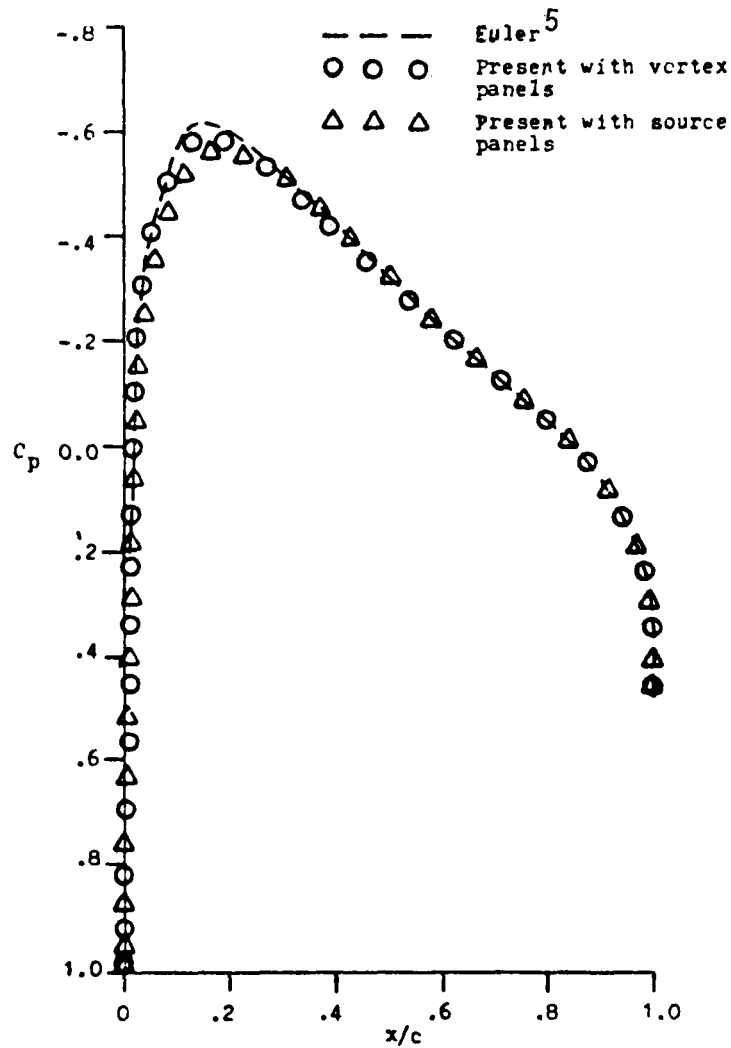

Fig. 19 Comparisons of IE Solution with Surface Vortex Panels and Surface Source Panels with Euler Solution, NACA 0012, $M_\infty = 0.72$, $\alpha = 0^0$.

First, we present a numerical test case to show the effect of introducing the shock panels and their fitting as explained earlier. Figure 20 shows a comparison between the shock capturing results and the SCSF-scheme results for the NACA 0012 airfoil at M_∞ = 0.8 and α = 0^0. It is clear that the SCSF-scheme sharpens the shock, as expected, with this relatively coarse grid. Next, we compare the SCSF-scheme with the experimental data and other computational results. Figure 21 shows the results of the SCSF-scheme for NACA 0012, M_∞ = 0.8 and α = 0^0, along with comparisons with the computational results of Garabedian, Korn and Jameson[6] and the experimental data taken from reference 7. The SCSF-scheme took 12 iteration cycles of shock capturing (SC) and 13 cycles of shock fitting (SF) to achieve convergence.
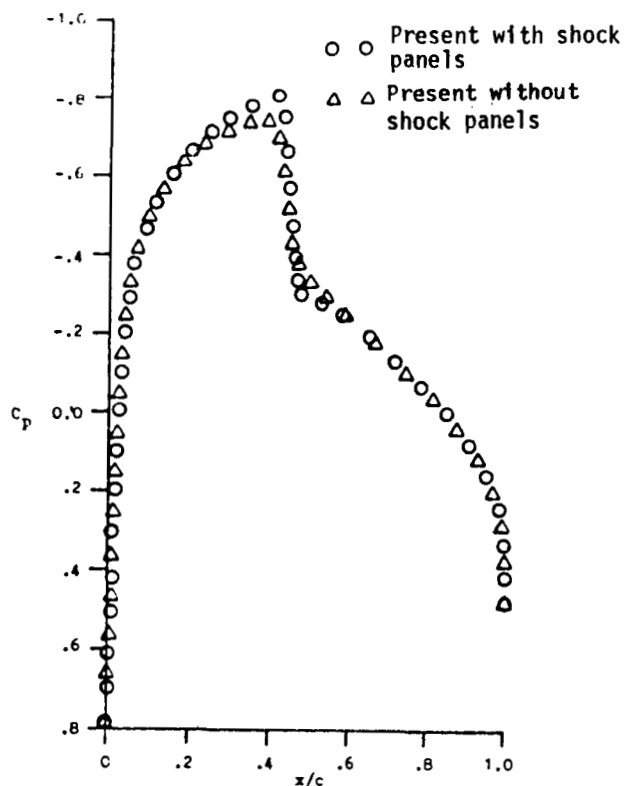

Fig. 20 Shock Capturing vz. SCSF-Scheme, NACA 0012, M_∞=0.8, α=0^0.

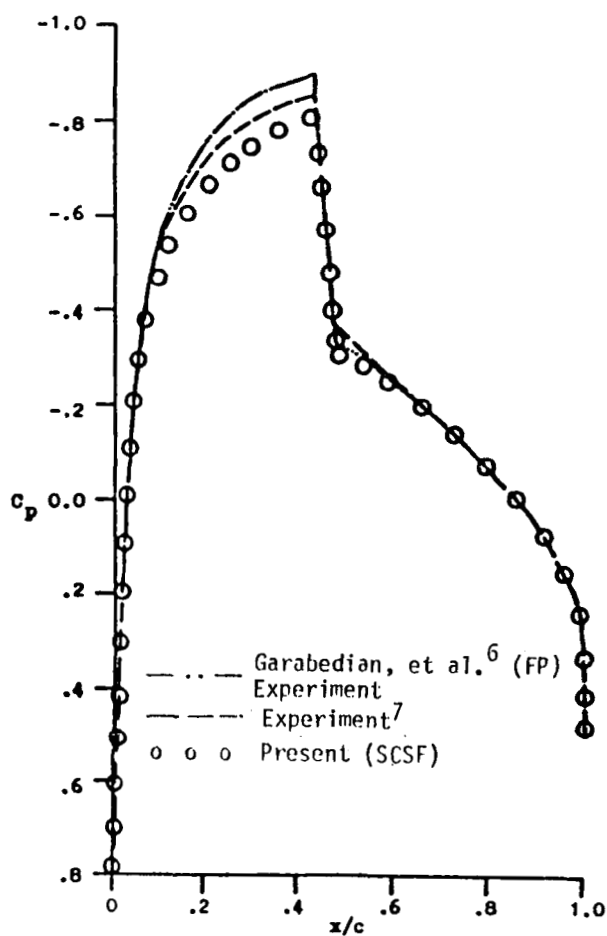Fig.21 Integral Equation Solution with SCSF-Scheme, NACA 0012, M_∞=0.8, α=0^0.

302

Figure 22 shows the results of the IFFE-scheme for the same case along with a comparison with the computational results of Jameson[8], who also used the finite-volume Euler scheme with four-stage Runge-Kutta time stepping. In the present IEEE-scheme, the embedded Euler domain has a size of 0.5x0.6 around the shock region with a grid of 25x30. This case took 10 iteration cycles of SC, 250 times cycles of Euler iterations to achieve a residual error of 10^{-3} and 5 IE cycles to update the Euler domain boundary conditions.

Fig.22 Integral Equation with Embedded-Euler Domain Solution, NACA 0012, $M_\infty=0.8$, $\alpha=0^0$.

Figures 23 and 24 show the results of the SCSF-and IEEE-schemes for NACA 64A010A, $M_\infty = 0.796$, $\alpha = 0^0$ along with comparisons with the computational results of Edwards, Bland and Seidel[9] who used the TSP-equation, and the experimental data taken from reference 9. With the SCSF-scheme, the numbers of SC and SF iteration cycles to achieve convergence are the same as those of the case presented in Figure 21. With the IEEE-scheme, the embedded Euler domain has a size of 0.7x0.6 with a grid size of 35x30. This case, Fig. 24, took 10 iteration cycles of SC, 130 time cycles of Euler iterations to achieve a residual error of 10^{-3} and 3 IE cycles to update the Euler domain boundary conditions.
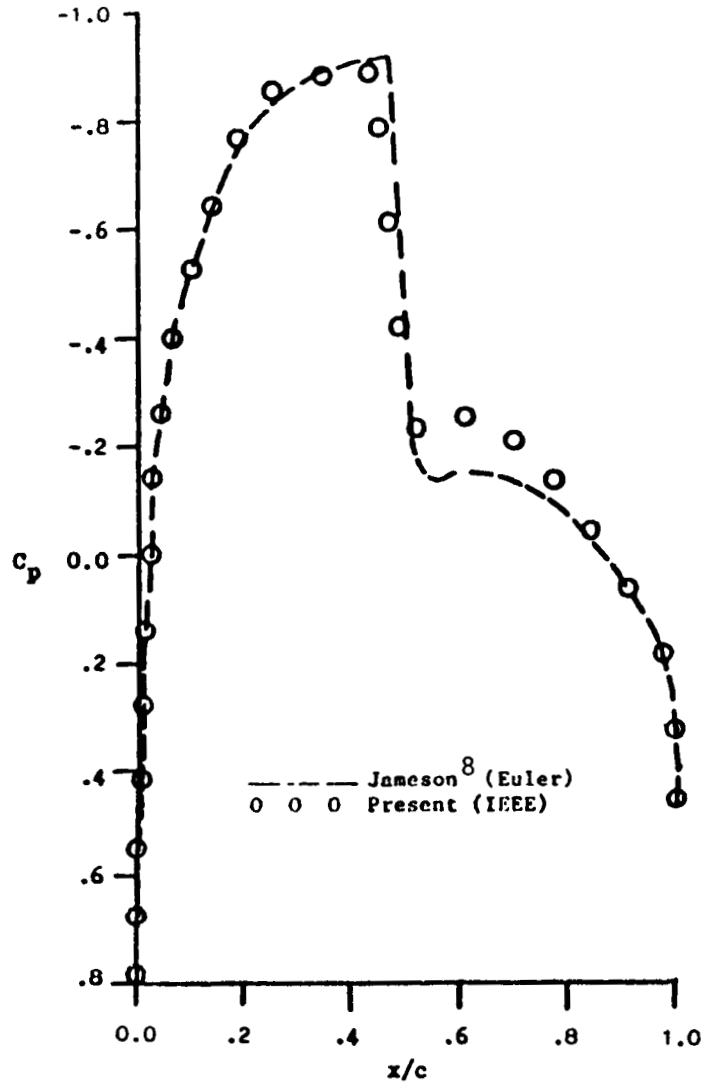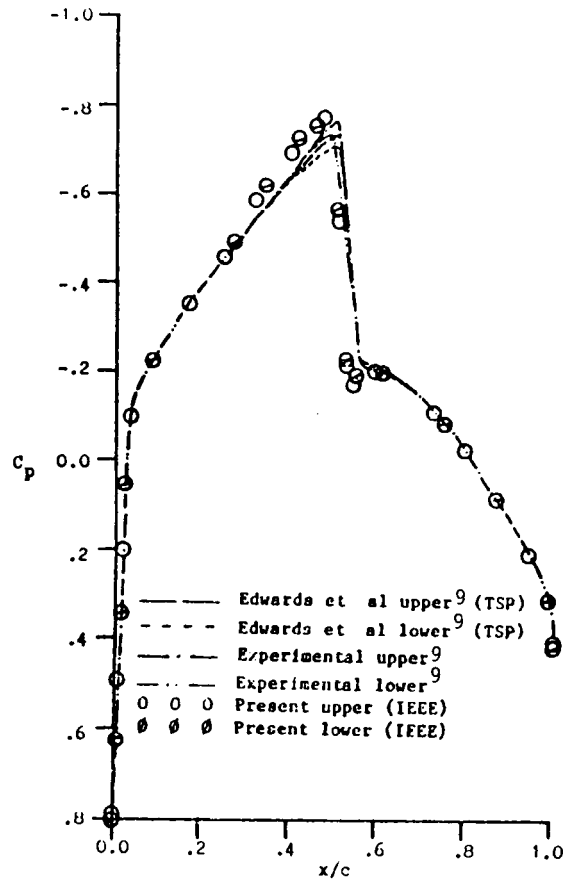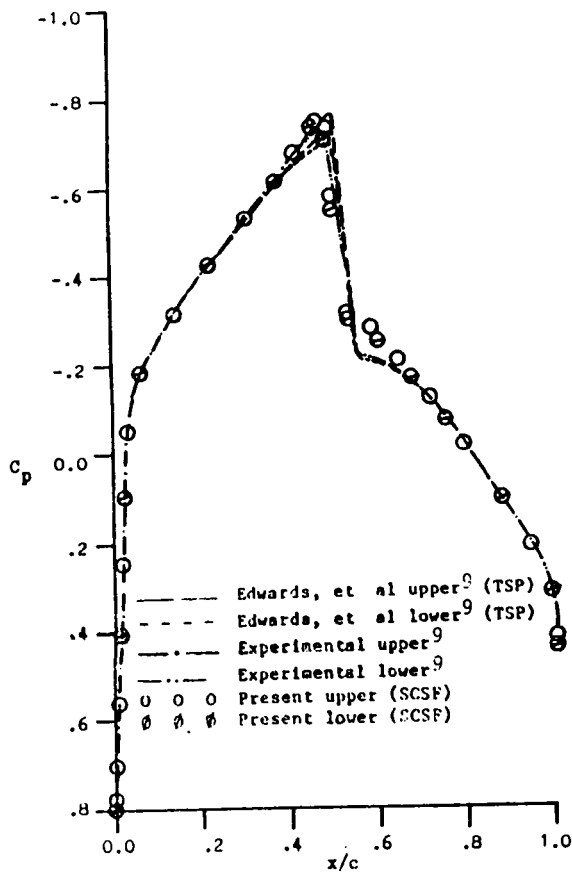

Fig. 23 Integral Equation Solution with SCSF-Scheme, NACA 64A010A, $M_\infty = 0.796$, $\alpha = 0^0$.

Fig. 24 Integral Equation with Embedded-Euler Domain Solution, NACA 64A010A, $M_\infty = 0.796$, $\alpha = 0^0$.

Figures 25 and 26 show the results of the SCSF- and IEEE-schemes for the lifting case of NACA 0012, M_∞ = 0.75 and α = 2^0 along with the computational results of Steger and Lomax[10], and the experimental data taken from the same reference. The size of the grids and the number of iteration cycles used to achieve convergence are the same as those of the cases given in Figures 21 and 22.
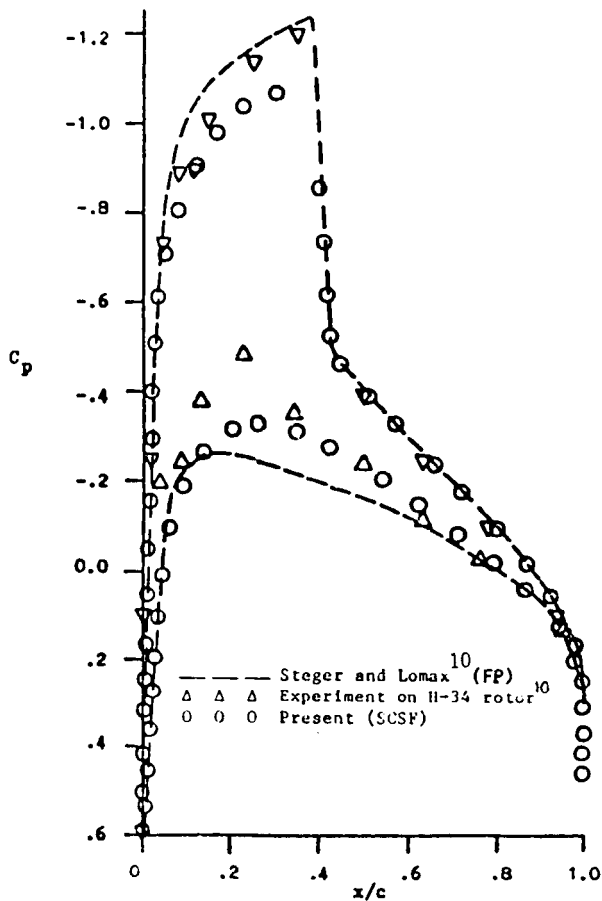

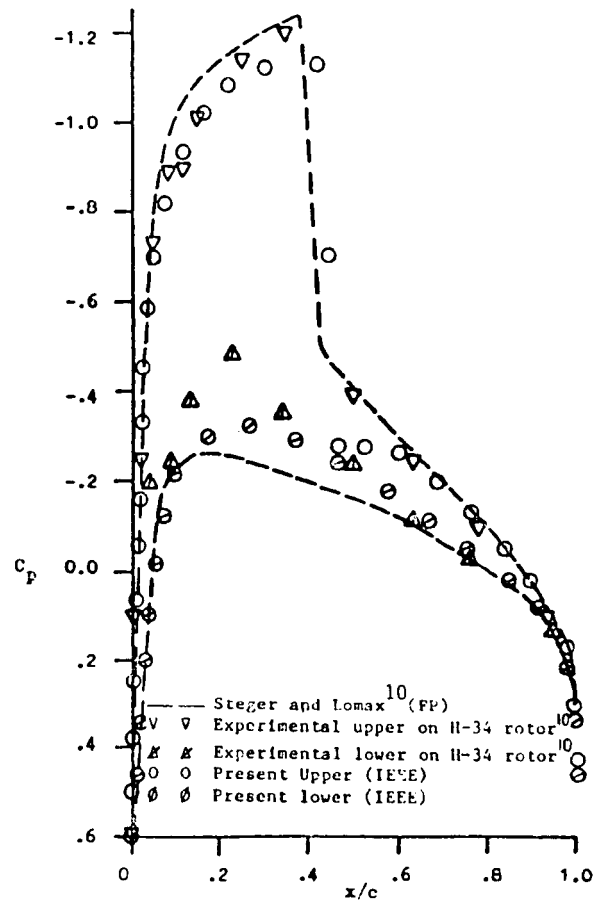Fig. 25 Integral Equation Solution with SCSF-Scheme, NACA 0012, M_∞=0.75, α=2^0.

Fig. 26 Integral Equation with Embedded-Euler Domain Solution, NACA 0012, M_∞=0.75, α=2^0.

For stronger shocks than those considered above the IE computational domain is extended in the longitudinal and lateral directions and so is the embedded Euler computational domain. The Euler domain is extended beyond the trailing edge to allow for the vorticity to be shed downstream where the overlapping region with the IE equation exists. Figure 27 shows a typical computational domain with details of the embedded Euler domain.
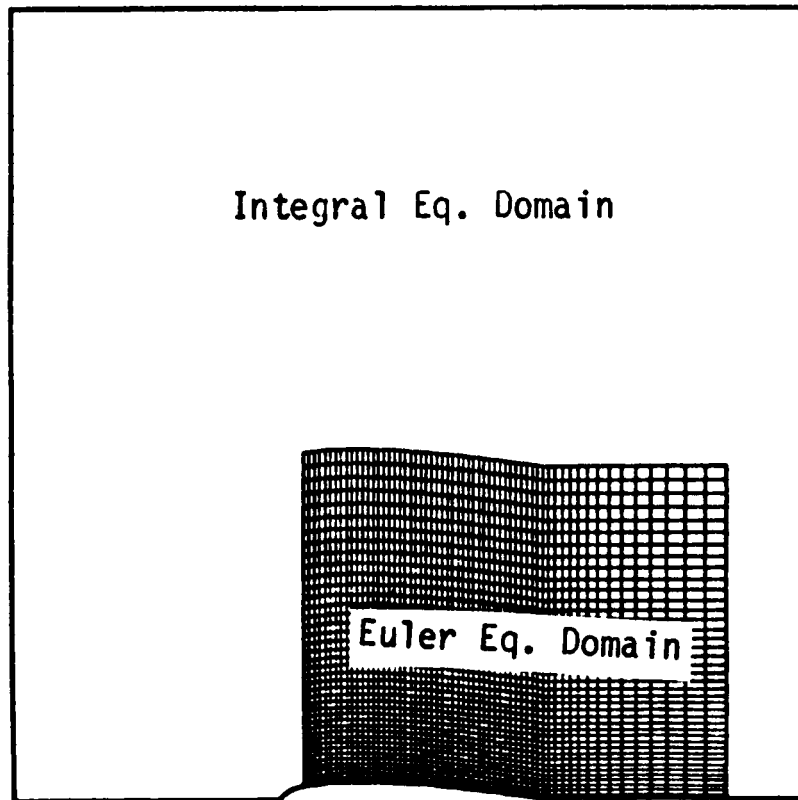

Fig. 27 Embedded Euler Domain and Grid for Strong Shocks.

Figure 28 shows the results of the IEEE for NACA 0012, M_∞ = 0.812 and α = 0^0 along with the experimental data of reference 7. In Figure 29, the results of the IEEE for NACA 0012, M_∞ = 0.82 and α = 0^0 are shown along with the three-dimensional solution at the wing root chord of Tseng and Morino[12], who use the IE for the TSP, and the results of reference 11. The size of the embedded Euler domain for these cases is 0.8x0.8 and its grid size is 40x40.
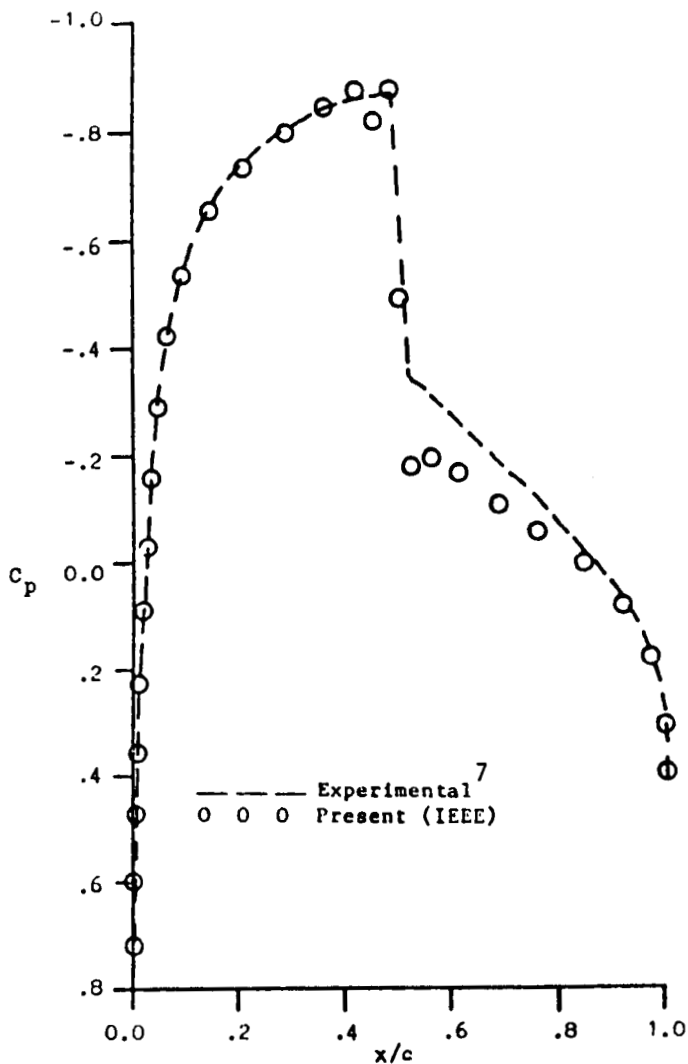

Fig. 28 Integral Equation with Embedded-Euler Domain Solution, NACA 0012, M_∞=0.812, α=0^0.

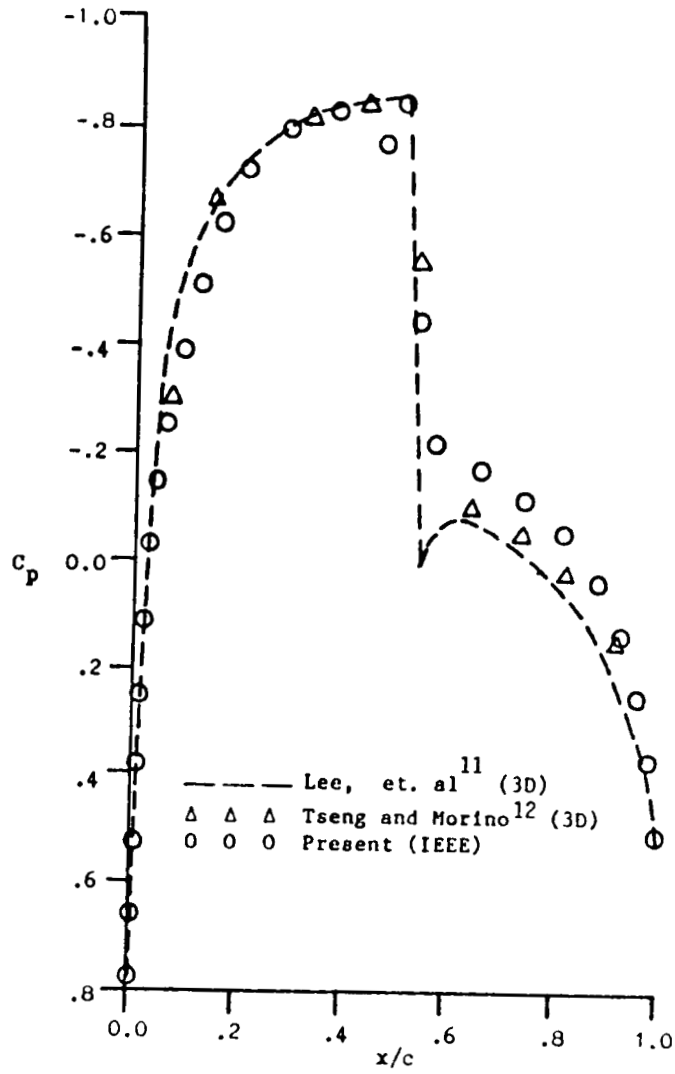Fig. 29   Integral Equation with Embedded-
Euler Domain Solution, NACA 0012,
$M_\infty = 0.82$, $\alpha = 0^0$.

Figure 30 shows the results of the IEEE for NACA 0012, $M_\infty = 0.84$ and $\alpha = 0^0$ along with comparisons with the nonisentropic FP-solution of Whitlow, et al.[13] and the Euler equations solution of Jameson[8]. The size of the embedded Euler domain for this case is 1.5x1.0 and its grid size is 60x40. This case took 10 IE iteration, 300 time cycles of Euler iterations and 3 IE cycles to update the Euler domain boundary conditions.
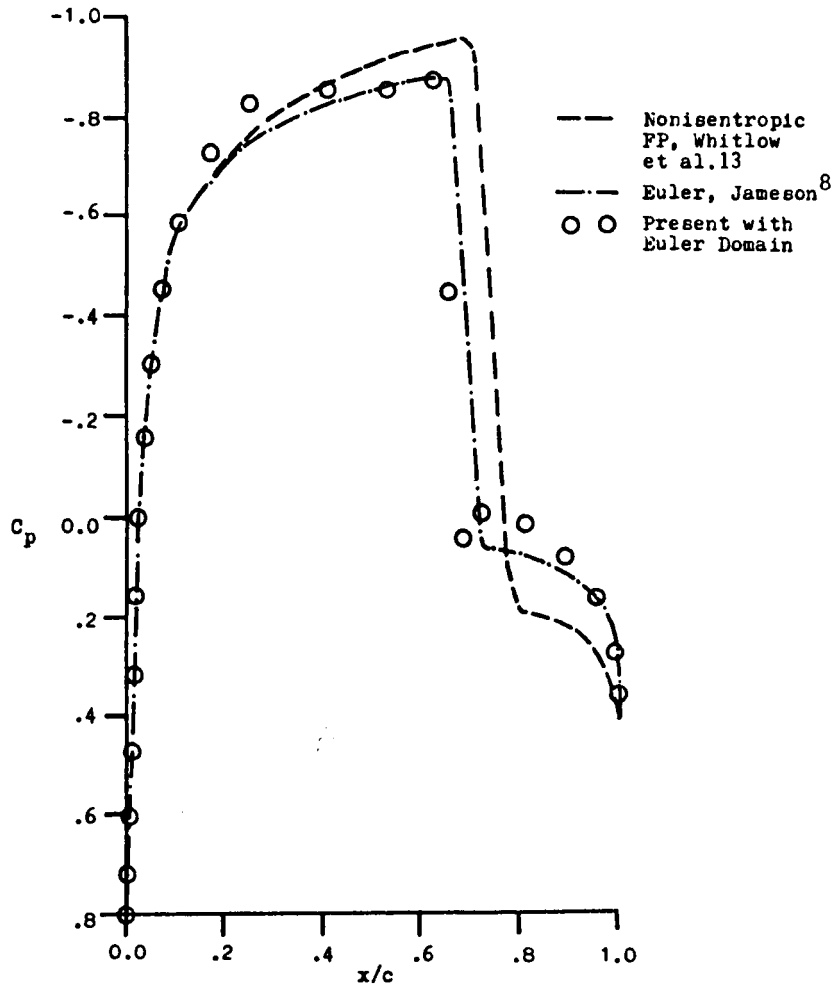

Fig. 30 Integral Equation with Embedded-Euler Domain Solution, NACA 0012, $M_\infty=0.84$, $\alpha=0^0$.

4. Concluding Remarks

- Two Methods have been Presented for Inviscid Transonic Flows:
  - Unsteady Euler Equations in a Rotating Frame of Reference for Transonic-Vortex Flows.
  - Integral Solution of Full-Potential Equation with and without Embedded Euler Domains for Transonic Airfoil Flows.

- The Computational Results Covered:
  - Steady and Unsteady Conical Vortex Flows
  - Three-Dimensional Steady Transonic Vortex Flow
  - Transonic Airfoil Flows

- The Results are in good agreement with Other Computational Results and Experimental Data.

- The Rotating Frame of Reference Solution is Potentially Efficient as Compared with the Space-Fixed Reference Formulation with Dynamic Gridding.

- The Integral Equation Solution with Embedded Euler Domain is Computationally Efficient and as Accurate as the Euler Equations.

- Currently the Rotating Frame of Reference Eule Solver is Applied to Three-Dimensional Unsteady Transonic-Vortex Flows. The IEEE-Scheme is Being Extended to the Unsteady Transonic Airfoil Calculations.

310

REFERENCES

1. Miller, D. S. and Wood, R. W.: Lee-Side Flow Over Delta Wings at Supersonic Speed. NASA TP-2430, 1985.

2. Kandil, O. A. and Chuang, A. H.: Influence of Numerical Dissipation in Computing Supersonic Vortex-Dominated Flows. AIAA Paper 86-1073, May 1986. Also to appear in the AIAA Journal, Vol. 25, No. 9, September 1987.

3. Rizzi, A., Eriksson, L. E., Schmidt, W. and Hitzel, S. M.: Simulating Vortex Flows Around Wings. AGARD CP No. 342, April 1983, pp. 21.1-21.14.

4. Hummel, D.: On the Vortex Formulation Over a Slender Wing at Large Angles of Incidene. AGARD CP-247, January 1979, pp. 15.1-15.17.

5. Sells, C. L.: Plane Subcritical Flow Past a Lifting Airfoil. Proceedings of the Royal Society, London, No. 308 (Series A), 1968, pp. 377-401.

6. Garabedian, P., Korn, D. G. and Jameson, A.: Supercritical Wing Sections. Lecture Notes in Economic and Mathematical Systems, Vol. 66, 1972.

7. Hall, M. G.: Transonic Flows. IMA, Controller, HMSO, London, 1975.

8. Jameson, A.: Transient Airfoil Calculations Using the Euler Equations. Numerical Methods in Aeronautical Fluid Dynamics (Ed. P. L. Roe), Academic Press, London and New York, 1982, pp. 289-309.

9. Edwards, J. W., Bland, S. R. and Seidel, D. A.: Experience with Transonic Unsteady Aerodynamic Calculations. NASA TM 86278, Langley Research Center, Hampton, VA, 1984.

10. Steger, J. L. and Lomax, H.: Transonic Flow about Two-Dimensional Airfoils by Relaxation Procedures. AIAA Journal, Vol. 10, 1972, pp. 49-54.

11. Lee, K. D., Dickson, L. J., Chen, A. W. and Rubbert, P. E.: An Improved Matching Method for Transonic Computations," AIAA Paper 78-1116, 1978.

12. Tseng, K. and Mornio, L.,: Nonlinear Green's Function Methods for Unsteady Transonic Flows. Transonic Aerodynamics (edited by D. Nixon), AIAA, New York, 1982, pp. 565-603.

13. Whitlow, W., Jr., Hafez, M. M. and Osher, S. J.: An Entropy Correction Method for Unsteady Full Potential Flows with Strong Shocks. NASA TM 87769, Langley Research Center, Hampton, VA, 1986.